Ptychography for Nonlinear Optical Microscopy

Evan Norris

Thesis submitted to the
Faculty of Graduate and Postdoctoral Studies
In partial fulfillment of the requirements
For the M.Sci. degree in Physics

Ottawa-Carleton Institute of Physics
Department of Physics
Faculty of Science
University of Ottawa
Ottawa, Canada

Summary

In this thesis I will introduce a novel nonlinear optical microscopy method to address some of the shortcomings in the current nonlinear optical microscopy literature and offer a supplement to traditional fluorescent microscopy for label free optical biomedical imaging. In order to demonstrate this method I describe a method for the generation of a numerical sample of collagen fibrils, produce a set of numerical diffraction measurements. I introduce a novel ptychography model for the simultaneous reconstruction of the components of the nonlinear optical susceptibility tensor and demonstrate the results of this model using numerically generated measurements from a numerical collagen sample. I additionally use the recovered information from ptychography to retrieve new information about the structure of a sample.

Statement of Originality

I hereby certify that all work presented in this thesis is my own.
Both the sample generation and the ptychography software were originally developed by Jarno van der Kolk (A previous Ph.D. student in our research group) however over the course of this project I have contributed additional features and fixes. The ptychography software used throughout this work is a new implementation of the software written previously with additional features developed to enable both readability and portability. The software development in this project aimed to address known problems in the ptychography software and the development of additional software for the preparation and analysis of data, these analytical scripts were written almost entirely by me with some assistance from both Jarno van der Kolk and my thesis advisor, Lora Ramunno.

Acknowledgements

I would like to thank everyone who assisted and supported me during my time working on this project. First and foremost I would like to thank Prof. Lora Ramunno, my thesis advisor. Thanks to her constant guidance I was able to become acquainted with both nonlinear optics and microscopy two areas that were unknown to me prior to beginning this project. I would also like to thank Dr. Jarno van der Kolk who was constantly lending a hand in the development of this project and assisting me when I ran into a wall developing or running software both locally and on our high performance computer. I would also like to thank my fellow group members who were willing to listen and help me find new solutions to problems as they arose.

Finally I would like to thank my family and friends in both Texas and Louisiana, who I'm sure weren't always thrilled by my decision to study so far away, for their constant support. I would also like to thank my partner Monyk for her help when I needed to figure out how to talk generally about my work and for putting up with me and my non-traditional hours during this project.

Table of contents

List of Figures

1

Introduction

There have been significant advancements in optical microscopy since the discovery of fluorescence by George G. Stokes in the middle of the nineteenth century. One of the most significant advancements in optical microscopy was the development of fluorescent dyes for labelling by Albert Coons in the early 1940s [1]. Fluorescence imaging has since become an indispensable tool in the life-sciences due to its sensitivity and high temporal and spatial resolution, down to the nanometer scale in some cases [2]. Some of the commonly used techniques in fluorescence microscopy techniques have been used to enable in vivo biomedical imaging [3, 4, 5], three-dimensional imaging [6, 7], and single cell imaging [8, 9]. The primary principle utilized by fluorescence microscopy is the emission of light from the excited singlet state of a substance that has absorbed electromagnetic radiation of a different wavelength [10]. Additionally the staining of a material with fluorescent dyes make it possible to apply this imaging process to materials that would otherwise not produce a necessary fluorescent signal.

Fluorescent imaging has seen further advancement beyond the diffraction limit in the past few decades. One notable method developed in 1994 is Stimulated Emission Depletion (STED) microscopy. This method is able to surpass the diffraction limit while still imaging in the far-field by employing targeted excitation and depletion beams to

"turn-off" fluorescence of regions surrounding an area of interest thus minimizing the illumination area at the focal point [11, 12]. Using STED microscopy imaging it is possible to image living cells beyond the diffraction limit allowing for further detail in diagnostic medical devices [13, 14]. While STED achieves resolution beyond the diffraction limit by actively tuning fluorescence signals there also exist numerical techniques for achieving such resolutions. One such method is Structured Illumination Microscopy (SIM) utilizes a set of images illuminated using multiple illumination patterns to exploit large-scale diffraction patterns known as moiré fringes [15, 16]. Stochastic methods for super-resolution include stochastic optical reconstruction microscopy (STORM) and photo-activated localization microscopy (PALM).STORM overcomes the diffraction limit by using multiple optical sources of different colors to illuminate only a fraction of fluorophores in the field of view at a time and then reconstruct a high resolution image using the set of discrete images [17, 18]. Alternatively PALM uses a set of photon distribution to determine molecular localization by statistically fitting an ideal point spread function to data collected by selectively activating small populations of fluorophores [19, 20]. Second Harmonic Generation (SHG) is the nonlinear optical process that occurs when a laser beam is incident upon a material whose second-order nonlinear susceptibility, $\chi^{(2)}$, is nonzero. SHG is the process by which two photons with identical frequency are combined to generate a new photon with twice the frequency (half the wavelength) of the initial photons while preserving the coherence of the excitation [21]. SHG offers high sensitivity to certain classes of ordered structures, often while producing virtually no detectable background from disordered media. As a consequence of this sensitivity SHG provides image contrast unique from what is achievable using conventional optical systems [22]. Second harmonic generated light, due to its coherence, is intrinsically sensitive to the structural organization of a material which allows for high contrast imaging ordered versus disordered structure and molecular orientation [23, 24]. Naturally it is necessary to describe why SHG possesses this sensitivity and what kind of materials can actually be imaged with it.

For SHG to occur two conditions must be met; a system must not have a center of inversion symmetry, and it have a large molecular hyperpolarizability. The hyperpolarizability of a molecule, $\overleftrightarrow{\beta}$ is a tensor that describes nonlinear scattering processes such as hyper-Raleigh scattering (HRS). HRS, which is categorized by phase and energy conservation, leads to the possibility of coherent summation of all waves scattered from all irradiated molecules. The signal generated by HRS however is dependent on the relative

orientation of all near molecules meaning that two molecules aligned parallel to each other will interfere constructively while two molecules aligned anti-parallel to each other will interfere destructively. In a population of molecules, the resulting signal will be the overall interference of all molecules rather than simply the sum of scattered powers. The coherent production of HRS (at half the pump frequency) when molecules are well aligned is Second Harmonic Generation [22].

Now that there is some basis for the sensitivity of SHG to molecular organization it is necessary to describe the kind of molecule that can be studied. The intrinsic SHG sources lie within the amine bonds of polypeptide chains, particularly the peptide bond, C-N, between two amino acids. As such the ability of a protein to generate SHG depends on its structure and folding, particularly the degree of alignment between peptide bonds. In helical structures peptide bonds tend to be very well organized. Thus, proteins with strong helical structures tend to produce strong SHG signals [22]. Collagen, which commonly forms into a triple-helical structure, has been shown experimentally to produce strong SHG signals.

The strong SHG production of collagen make it an ideal molecule to study with SHG. So, it is prudent to describe what kinds of information can be gained from studying collagen. Collagen is the most abundant protein in animals [25], as it plays an important role in the in the formation of tissues and organs. Collagen is studied widely in biomedical applications due to its potential to serve as a diagnostic marker for various pathological processes and diseases, such as cancer, the healing of wounds, and osteoarthritis [26, 2, 27]. The structure and organization of collagen fibrils plays a significant role in its application as a diagnostic marker, and as such, the development of imaging methodologies to better study these factors is of great importance to the field of biomedical imaging. Gaining access to this information however has its own complications. The orientation of a molecule is linked to the phase of the produced SHG signal, specifically the phase of the SHG signal inverts when the orientation of the molecule flips [22], However, optical detectors are able to measure only the intensity of an incident signal, and thus retrieving phase information is not possible with standard SHG microscopy.

In order to solve this phase problem, a novel microscopy technique has been introduced called interferometric Second Harmonic Generation (iSHG). As its name implies iSHG employs the principle of interferometry to recover phase information about a sample. In general iSHG is accomplished by mixing the SHG signal generated from a sample of interest with a reference signal generated by a crystal capable of producing strong

SHG signals [28]. The mixing of sample and reference signals is achieved by implementing a Michelson interferometer into the optical configuration. Presently iSHG has found application in the imaging of collagen fibrils [29, 30] with the objective being to retrieve the polarity of fibrils in a sample. The primary limitation of iSHG is the requirement of a stable reference beam common to all interferometry derived methods, additionally with this requirement only fibril polarity can be inferred from the recovered phase information, additionally this method is restricted to confocal geometries and require many repeated measurements to retrieve phase information.

In order to gain more robust information about a collagen alignment, one may use polarization SHG (pSHG), which involves modulating incident polarization of radiation striking a sample. The detected SHG intensity then provides a characteristic modulation which can be used to obtain orientation information otherwise unreachable with SHG intensity measurements [31]. This method is however limited by the size of collagen fibrils which are smaller than the optical resolution which makes it difficult to study collagen arrangement at scale [32]. This method additionally requires a fairly robust optical system and a large number of measurements which can become prohibitive requirements in some cases.

One of the shortcomings of both ISHG and PSHG are their restriction to confocal geometries which require small spot sizes which in turn requires many measurements to produce an image. Alternatively wide-field imaging allows for much faster image acquisition due to the use of much larger spot sizes to illuminate large sections of a sample [33]. While the potential resolution of confocal microscopes is very high in practice there is very little difference between the achievable resolution in confocal and wide-field microscopes [34]. SHG can be used with wide-field imaging, removing the traditional limits of the confocal geometry and in turn allowing larger samples to be imaged [35, 36].

In this thesis we propose a new computational technique microscopy technique for nonlinear optical microscopy based on ptychography, which allows us to retrieve the phase and orientation of collagen samples via a set of diffraction images taken with much larger spot sizes than allowed by confocal geometries. Ptychography is a computational phase recovery technique that can deployed without the need of high quality lenses and without interferometry. This method was introduced to solve the phase problem in way that both bypasses problems introduced by low quality lenses and improves spatial resolution [37]. Ptychography works by capturing light scattered by a sample directly onto a CCD camera with or without the use of a collecting lens. By using multiple, overlapping far-field

intensity patterns generated from random points within a sample it is possible, using a numerical algorithm, to reconstruct the transmission function. In this work I will describe a framework for expanding ptychographic reconstruction to support general nonlinear optical imaging techniques and utilize it to discern information about sample structure and organization while benefiting from the reduced number of measurements allowed by wide-field imaging. It was demonstrated in [38, 39] that nonlinear ptychography is capable of reconstructing the phase of the second order nonlinear susceptibility and in [40, 41] it was shown that it is possible to reconstruct multiple vector components of a linear optical transmission function. I present in this work a method that combines and extends the reconstruction of the second order nonlinear susceptibility and the ability to reconstruct multiple components of an object function to build a novel model that is able to reconstruct multiple tensorial components of the second order nonlinear susceptibility.

This thesis is organized as follows. In the second chapter I discuss the structure of collagen samples and detail a methodology for computationally generating a sample of overlapping collagen fibrils that can be used to generate numerical far field measurements, and the method for retrieving information about structure and alignment if the spatially-dependent second order nonlinear optical susceptibility is known. In the third chapter I will introduce the tensorial Ptychographic Iterative Engine (tPIE), which establishes a framework by which a generalized ptychography algorithm can be employed to reconstruct any nth order nonlinear optical susceptibility from either simulated measurements of a sample (what we do here, and which is also described in chapter 3) or from experimental measurement data. In the fourth chapter I present our main results, wherein we apply our tPIE algorithm to the reconstruction of the second order nonlinear optical susceptibility of a numerical collagen sample. We first apply our sample generation model to produce the numerical sample, then create numerical measurements of diffraction patterns, then compare our reconstructed nonlinear susceptibility components to that of the original numerical sample. Finally, I show that the orientation and relative polarity of the collagen fibril sample can be retrieved from the ptychographic reconstructions, with fewer measurements that would be required in other methods. I demonstrate that our methodology is able to reliable and accurately reconstruct the components of the $\chi^{(2)}$ tensor and using this reconstructed information I demonstrate that information about sample orientation can be retrieved. In the final chapter present a summary and future work where we hope to further optimize the operation speed of this model, apply the techniques to imaging modalities beyond SHG, and design techniques for the

implementation of this model to experimentally acquired measurement data.

2

Numerical Generation and Characterization of Collagen Samples

2.1 Collagen Sample Generation

Fibrillar collagen is a material very important for biomedical imaging due to its potential to serve as a diagnostic marker for various pathological processes and its strong Second Harmonic Generation (SHG) response. The alignment of fibrillar collagen acts as a biomarker for the process of ageing, various pathological processes, and diseases, such as cancer and the healing of wounds [26, 2, 27]. There is a characteristic change in the organization of fibrillar collagen associated with several diseases, Imaging this change in orientation can act as a valuable early diagnostic marker [42] The organization of collagen has been imaged in the past using SHG microscopy [42, 43, 44], Forward/Backward SHG [45, 46], Interferometric SHG (ISHG) [30, 47, 48], Polarization SHG (PSHG) [32, 49], each of these methods either require a stable reference beam (ISHG), a large number of images (PSHG), or are not able fully retrieve information about the organization (SHIM, forward/backward SHG).

The purpose of this project is to design a new method that is able to address the short-

comings of the current imaging methodologies. In order to evaluate this novel imaging method, we create a "numerical sample" of collagen tissue, perform "numerical measurements" to obtain the corresponding far field SHG diffraction patterns, then use these measurements to reconstruct our sample via the new computational imaging method we have devised. By comparing the reconstruction to the original sample, we can then ascertain the validity of our approach.

The first step is to create a computer generated collagen sample, which is now what we describe in detail. The physical sample we are modelling consists of an ensemble of collagen fibrils located at various locations in space, with various orientations and polarity. The corresponding numerical sample for our numerical experiment is the spatially-dependent second-order nonlinear optical susceptibility tensor of the entire ensemble. We denote this by tensor by $\chi^{(2)}_{ijk}$, which we take to be in the laboratory reference frame (x, y, z).

The second order nonlinear response of an individual fibril is described by the hyperpolarizability tensor, whose elements we denote by β_{ijk} [21]. While it has 27 possible components, molecules with inherent symmetries will have a much smaller number of independent components. Collagen fibrils have $C_\infty mm$-symmetry along the fibril which reduces the number of independent components from 27 to 3. In addition, since the second harmonic wavelength commonly used (400nm) is far from the wavelength of the first electronic transition in collagen, we may assume that Kleinman symmetry also applies [50]. This further reduces the total number of independent components to 2. Under these assumptions, the second order nonlinear response for a collagen fibril oriented along the y axis can be expressed in a contracted tensor notation for β_{ijk} using the d-matrix,

$$d = \begin{bmatrix} 0 & 0 & 0 & 0 & 0 & d_{16} \\ d_{16} & d_{22} & d_{16} & 0 & 0 & 0 \\ 0 & 0 & 0 & d_{16} & 0 & 0 \end{bmatrix} \tag{1}$$

where the only independent, non-zero components of β_{ijk} in the molecular frame are β_{yyy} and $\beta_{xxy} = \beta_{xyx} = \beta_{yxx} = \beta_{yzz} = \beta_{zyz} = \beta_{zzy}$. [42]. The hyperpolarizability tensor described by eq 1 is for a fibril oriented along the y-axis in the laboratory frame. In order to describe the hyperpolarizability of a fibril with any possible orientation in space, we need a transformation matrix that will rotate the fibril accordingly. Because of the assumed cylindrical symmetry of the fibril, when the fibril is rotated about the y-axis there is no change in its orientation. Thus only two rotations are required to bring the fibril to any arbitrary orientation. The first rotation of the fibril through

angle θ about the x-axis (in the counter-clockwise direction, according to the right hand rule). Such a rotation will transform a point (x, y, z) to a new location given by $x'' = x$, $y'' = y\cos\theta - z\sin\theta$, and $z'' = y\sin\theta + z\cos\theta$. The second is a rotation of the fibril through angle ϕ about the z''-axis which will transform a point (x'', y'', z'') to a new location $x' = x''\cos\phi - y''\sin\phi$, $y' = x''\cos\phi - y''\sin\phi$, and $z' = z''$.

The effect of the two rotations on fibril orientation are illustrated in Fig 1, where the laboratory frame is shown inn red, and the molecular reference frame of the fibril after the θ and ϕ rotations is shown in blue. The original fibril position was along the y-direction of the laboratory frame, whereas its final position after the two rotations is along the y'-axis and is depicted by the green cylinder in the figure.

Without loss of generality, we choose θ to take values between $-\frac{\pi}{2}$ and $\frac{\pi}{2}$, and ϕ to take values between 0 and 2π. The angle θ signifies the degree of alignment of the fibril with the laser propagation axis (which, recall, is the z-axis). For $\theta = 0$, the fibril is perpendicular to the z-axis, and will lie in the laboratory xy-plane, along a direction which is rotated ϕ from the y-axis. Whereas for $\theta = \pm\frac{\pi}{2}$, the fibril will like parallel to the z-axis. The angle ϕ signifies the degree of rotation away from the y-axis, in a plane perpendicular to z. From the two rotations described we can write the following rotation matrix

$$\overleftrightarrow{R} = \begin{bmatrix} \cos(\phi) & -\sin(\phi)\cos(\theta) & \sin(\phi)\sin(\theta) \\ \sin(\phi) & \cos(\phi)\cos(\theta) & -\cos(\phi)\sin(\theta) \\ 0 & \sin(\theta) & \cos(\theta) \end{bmatrix} \tag{2}$$

that transforms a point $\vec{r} = (x, y, z)$ in the laboratory frame to a new location $\vec{r}' = (x', y', z') = \overleftrightarrow{R}\vec{r}$, other vectors can be similarly transformed, as can tensors, however, the number of times $\overleftrightarrow{R}$ is applied depends on the dimensionality of the tensor. The components of the second order nonlinear susceptibility of a rotated collagen fibril is then given by

$$\tilde{\beta}^{(2)}_{i'j'k'} = R_{i'i}R_{j'j}R_{k'k}\beta_{ijk} \tag{3}$$

where we have used tensor notation with implied summation over repeated indices. Writing these components out explicitly, for the β_{ijk} tensor defined by Eq. 1 we obtain

$$\tilde{\beta}_{xxx} = -\sin^3\phi\cos^3\theta\beta_{yyy} + 3(\sin^2\phi\cos^2\theta - 1)\sin\phi\cos\theta\beta_{yxx} \tag{4}$$

$$\tilde{\beta}_{xxy} = \tilde{\beta}_{xyx} = \tilde{\beta}_{yxx} = \sin^2\phi\cos\phi\cos^3\theta\beta_{yyy} - (3\sin^2\phi\cos^2\theta - 1)\cos\phi\cos\theta\beta_{yxx} \tag{5}$$

$$\tilde{\beta}_{xyy} = \tilde{\beta}_{yxy} = \tilde{\beta}_{yyx} = -cos^2\phi\sin\phi\cos^3\theta\beta_{yyy} + (3\cos^2\phi\cos^2\theta - 1)\sin\phi\cos\theta\beta_{yxx} \tag{6}$$

$$\tilde{\beta}_{yyy} = \cos^3\phi\cos^3\theta\beta_{yyy} - 3(\cos^2\phi\cos^2\theta - 1)\cos\phi\cos\theta\beta_{yxx} \tag{7}$$

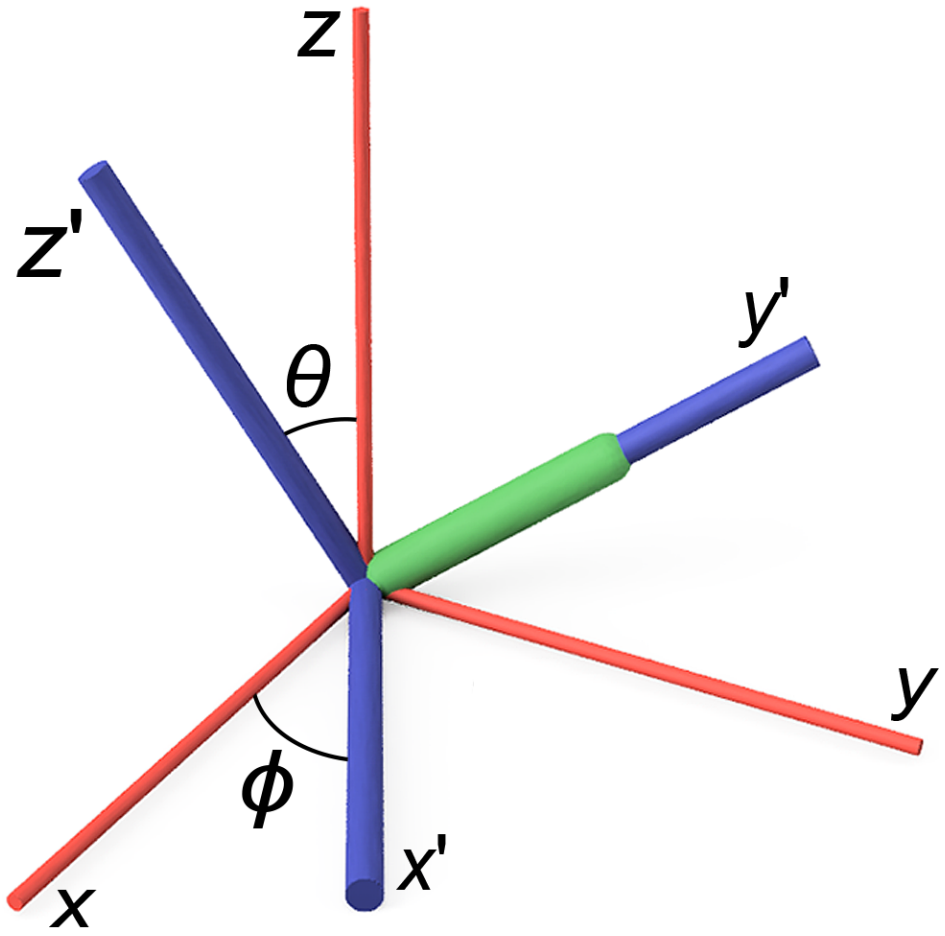

Figure 1: A collagen fibril is oriented along the y-axis of the molecular frame (x',y',z') which is rotated in plane by ϕ and out of plane by θ with respect to the laboratory frame (x,y,z)

$$\tilde{\beta}_{xxz} = \tilde{\beta}_{xzx} = \tilde{\beta}_{zxx} = \sin^2\phi\cos^2\theta\sin\theta\beta_{yyy} + (1 - 3\sin^2\phi\cos^2\theta)\sin\theta\beta_{yxx} \tag{8}$$

$$\tilde{\beta}_{xzz} = \tilde{\beta}_{zxz} = \tilde{\beta}_{zzx} = -\sin\phi\cos\theta\sin^2\theta\beta_{yyy} + (2 - 3\cos^2\theta)\sin\phi\cos\theta\beta_{yxx} \tag{9}$$

$$\tilde{\beta}_{zzz} = \sin^3\theta\beta_{yyy} + 3\sin\theta\cos^2\theta\beta_{yxx} \tag{10}$$

$$\tilde{\beta}_{yyz} = \tilde{\beta}_{yzy} = \tilde{\beta}_{zyy} = \cos^2\phi\cos^2\theta\sin\theta\beta_{yyy} + \sin\theta(1 - 3\cos^2\theta\cos^2\phi)\beta_{yxx} \tag{11}$$

$$\tilde{\beta}_{yzz} = \tilde{\beta}_{zyz} = \tilde{\beta}_{zzy} = \cos\phi\cos\theta\sin^2\theta\beta_{yyy} + (3\cos^2\theta - 2)\cos\phi\cos\theta\beta_{yxx} \tag{12}$$

We now describe how we generate $\chi^{(2)}_{ijk}$ that describes the second order nonlinear response of the entire ensemble of collagen fibrils that constitute our computational sample. In our numerical measurements described in the next chapter, we will linearly polarized beams propagating in the z-direction as well as a sample that is 2D in the xy plane. Thus only the first four components listed will contribute. The first stage is to randomly

place fibrils in a defined region and rotate them according to θ and ϕ, which are chosen according to the desired distribution. As a first test, we choose $\theta = 0$, and take ϕ to be uniformly distributed between 0 and $\frac{\pi}{4}$.

Collagen fibrils have β_{yyy} and β_{yxx} that are either "positive" or "negative" due to the microscopic details underlying the chirality of the collagen proteins. Due to the way in which collagen fibrils assemble, this property is preserved along hundreds of microns along the length of the fibril [51]. Collagen tissue is thus often characterized by the ratio of the average number of fibrils with positive β_{yyy} and β_{yxx} to the total number of fibrils. This ratio is defined as

$$f = \frac{N_+}{N_+ + N_-} \tag{13}$$

where N_+ and N_- refer to the number of fibrils with positive and negative β_{yyy} and β_{yxx} respectively. By varying the f-ratio, the average alignment of a sample can be controlled. For example, in a sample where there are multiple fibrils with the same orientation in space, when the f-ratio is 0.5 there would be on average an equal number of positive and negative fibrils and no general alignment exists.

We create a numerical collagen sample by introducing a "local" f-ratio in which the f-ratio varies linearly along the x-direction of our sample from $\bar{f}$ on one side to $(1 - \bar{f})$ on the other. We set $\bar{f} = 0.6$, as then our range includes f values measured for rat tail tendon [48]. Our local f-ratio is given by

$$f_{local} = \bar{r}\frac{x + 0.5L_x}{L_x} + (1 - \frac{x + 0.5L_x}{L_x})(1 - \bar{f}) \tag{14}$$

where L_x is the length of the sample in the x-direction, and determines the horizontal length of the box in which fibrils can be placed. To assign whether or not a fibril is positive or negative, f_{local} is then compared with a uniform random number between 0 and 1, if it greater than this random number this ϕ is increased by π. Thus ϕ not only accounts for how the fibril is rotated in space, but also contains its information about whether it is "positive" or "negative".

Each fibril is also given a diameter and length. The samples used in this work contain fibrils with uniform length of 10 microns and uniform diameter of 0.1 microns; it is however possible to vary both length and diameter of each fibril within our framework, but for simplicity these parameters remain constant. See fig 2 for an example image generated from the random placement and rotation of 30,000 collagen fibrils. Once this list of fibrils has been generated an image of the sample is rasterized, converted

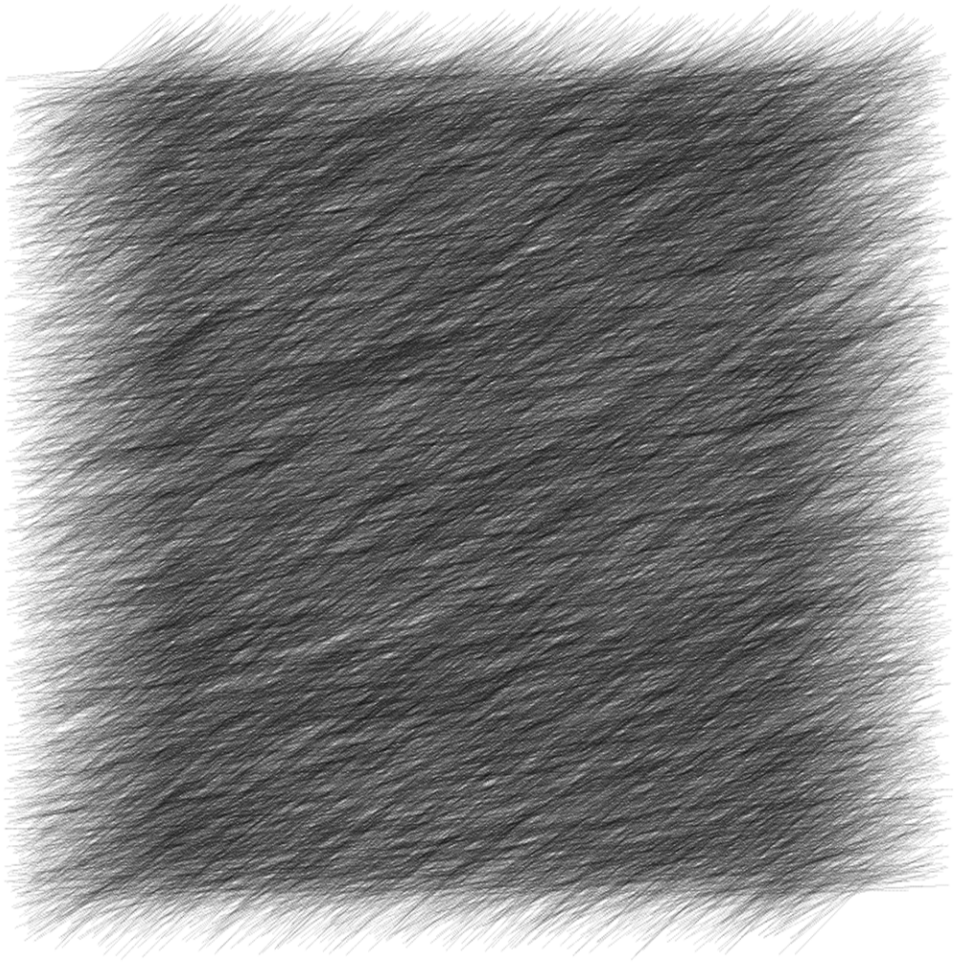

Figure 2: Computationally generated collagen sample with 30,000 randomly placed fibrils

from a list of fibrils and their attributes (location, rotation angles, length, width) to a pixelated image of fibrils in their respective locations via a raster scan. However to find the components of the nonlinear susceptibility of a sample the following process occurs during rasterization. For each pixel the in the image, every fibril is checked for overlap with every other fibril and the value of the nonlinear susceptibility for a given pixel is calculated as the sum of the contribution of every overlapping fibril in the pixel. A fibrils contribution is determined by the total percentage of the pixel that it occupies. The process is repeated for every fibril in every pixel of the image.

How the overlap impacts two aligned fibrils and two un-aligned fibrils is illustrated schematically in the below figure, which contains a horizontal reference fibril and a second rotated fibril. The coloring of a fibril corresponds to its alignment. As the alignment shifts, the color shifts from red when parallel to the reference fibril, to white when perpendicular to the reference fibril, to blue when anti-parallel to the reference fibril.

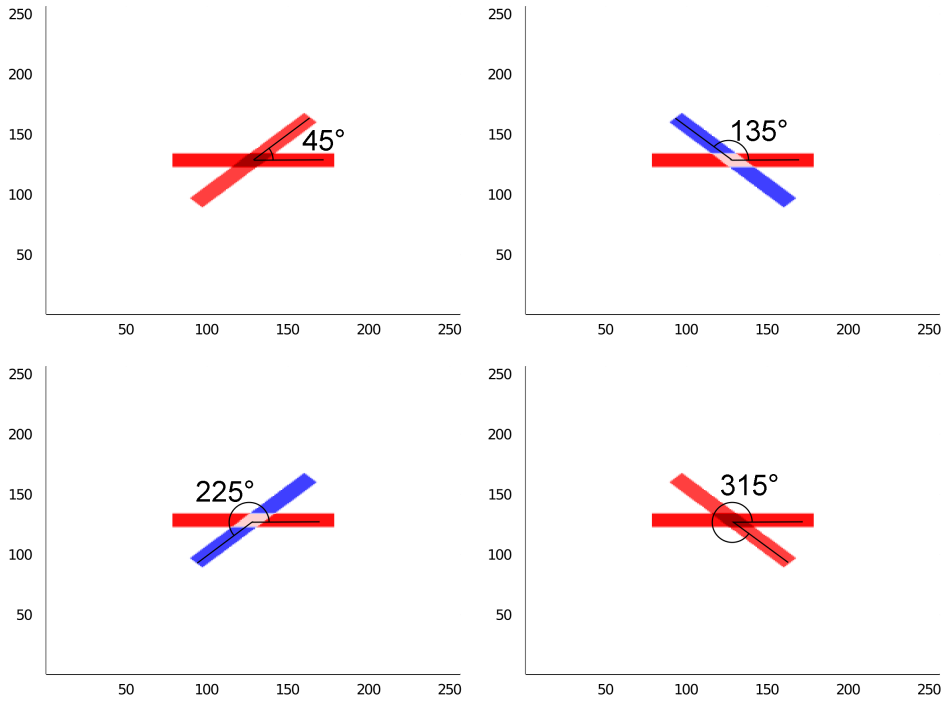

Figure 3: The value of $\chi^{(2)}_{ijk}$ in pixels with overlapping fibrils is the sum of their $\chi^{(2)}_{ijk}$ values

Once the sample has been rasterized it is separated into four complex arrays, one for each $\chi^{(2)}_{ijk}$ component of interest. The magnitude and phase of the rasterized $\chi^{(2)}_{ijk}$ samples are plotted separately and we refer to them as "original" images. These original images can be used as a best case scenario of any imaging process as they are diffraction unlimited and contain no defects. We have developed a framework for both the computational generation of a sample of collagen fibrils which can then be rasterized into sample images for four independent components of the nonlinear optical susceptibility tensor to be used in a computational second harmonic generation imaging algorithm.

2.2 Retrieval of Fibril Orientation

In the previous section, we described how a collagen sample (that is, the amplitude and phase of the xxx, xxy, xyy, and yyy components of the $\chi^{(2)}$ tensor for a sample composed of many collagen fibrils) are generated and rasterized. The rasterized images do not contain information about each individual fibril, but rather they are composed of pixels in the xy-plane. The $\chi^{(2)}$ values for a particular pixel are a weighted average of the corresponding $\tilde{\beta}$ values from all the fibrils that overlap in space with that pixel. Thus, the rasterized image represents an averaging over the sample.

In order to retrieve the average orientation of the fibrils contained in a pixel, we assume that the $\chi^{(2)}$ components for an individual pixel in a rasterized sample describe a single effective pixel, and it is the orientation of this effective pixel that we seek. Assuming that we know $\chi^{(2)}_{xxx}$, $\chi^{(2)}_{xxy}$, $\chi^{(2)}_{xyy}$, and $\chi^{(2)}_{yyy}$ for a pixel, then we can recover the rotation angles ϕ and θ of this single effective fibril by inverting Eqs [4-7]. This procedure can be applied to the rasterized $\chi^{(2)}$ images for our numerical sample, as well as ptychographically reconstructed $\chi^{(2)}$ images (discussed in chapter 3). It is important to note that it is not possible to retrieve orientation information about a specific fibril in the sample but rather only the "effective fibril" which corresponds to all fibrils overlapping on a given pixel. This effective fibril orientation provides information about the overall orientation of a particular region rather than about an individual real fibril itself.

While the original rasterized sample $\chi^{(2)}$ images are all real valued, the ptychographically $\chi^{(2)}$ images reconstructed from diffraction patterns are in general complex, we denote these complex values as $\tilde{\chi}^{(2)}_{xxx}$, $\tilde{\chi}^{(2)}_{xxy}$, $\tilde{\chi}^{(2)}_{xyy}$, and $\tilde{\chi}^{(2)}_{yyy}$. Essentially, the $\chi^{(2)}$ components are reconstructed such that the relative phase between complex components is correct, but there is in general a global phase factor applied to each component that makes it different from the (real-valued) originals.

Thus, the first step is to identify and remove this global phase factor to produce $\chi^{(2)}$ images that are (essentially) real-valued, since Eqs. [4-7] are valid when quantities on the left hand side are real valued. To compute this phase factor, we enforce the following condition at each location and for each component

$$Im[\tilde{\chi}^{(2)}_{ijk}\exp(i\alpha)] = 0 \tag{15}$$

where α denotes the phase factor, and is a real-valued number. This condition then gives

$$\tan(\alpha) = -\frac{Im[\tilde{\chi}^{(2)}_{ijk}]}{Re[\tilde{\chi}^{(2)}_{ijk}]} \tag{16}$$

As anticipated, we found that the values of α obtained for each component in each pixel are nearly the same, and $\tilde{\chi}^{(2)}_{ijk}\exp(i\alpha)$ is very nearly a real number in practice. However, to apply Eqs. [4-7], we need quantities on the LHS that are exactly real valued. Thus we take the real part explicitly, that is, we set $\chi^{(2)}_{ijk} = Re[\tilde{\chi}^{(2)}_{ijk}\exp(i\alpha)]$.

As mentioned in the previous section, when a pixel contains N fibrils that overlap with it, the $\chi^{(2)}$ components for that pixel will be the sum of the $\tilde{\beta}^{lab}$ components for each fibril, each weighted by a particular weighting factor w. Thus the $\chi^{(2)}_{ijk}$ component for a pixel is given by

$$\chi^{(2)}_{ijk} = \sum_{n=1}^{N} w_n (\beta^{lab}_{ijk})_n \tag{17}$$

Where the subscripts n enumerate the N overlapping fibrils. Of course, when generating a sample, each of the N fibrils overlapping a pixel will in general have distinct θ and ϕ values, where their "positive" and "negative" status is implicitly contained within ϕ. However, if we only have the $\chi^{(2)}_{ijk}$ values, we have no way of determining what the underlying fibrils are. We thus treat the entire pixel as an "effective single fibril," by assuming that all fibrils contained in the pixel have the same ϕ and θ value, but leave open the possibility that some will be "positive" and some will be "negative." Since collagen fibrils are such that the signs of β_{yyy} and β_{yxx} are either both positive, or both negative, we can then re-write the sums over fibrils in eq 17 in the form

$$\chi^{(2)}_{ijk} = f_{ijk}(\phi, \theta) \sum_{n=1}^{N} w_n (sign(\beta_{yyy}))_n \tag{18}$$

where $f_{ijk}(\phi, \theta)$ are the right hand sides of Eqs. [4-7] for a single fibril, but with the sign of β_{yyy} taken out. For example, for the xxx component we have

$$f_{xxx}(\phi, \theta) = -\sin^3\phi\cos^3\theta|\beta_{yyy}| + 3(\sin^2\phi\cos^2\theta - 1)\sin\phi\cos\theta|\beta_{yxx}| \tag{19}$$

Where $|\beta_{yyy}|$ and $|\beta_{yxx}|$ are known quantities, which have values of 0.7 and 0.3, respectively, for collagen fibrils [42]. It is these functions $f_{ijk}(\phi, \theta)$ that we assume to be the same for each fibril that would be overlapping in a pixel.

The quantity multiplying the $f_{ijk}(\phi, \theta)$ is the same for each component, and thus can be understood as an effective amplitude of the second order response of that pixel, that is

$$A = \sum_{n=1}^{N} w_n (sign(\beta_{yyy}))_n \tag{20}$$

if, for example, we have two fibrils overlapping in a pixel, with the same alignment and same weighting, but one is "positive" and one is "negative," the we would expect zero nonlinear response from that pixel, and indeed the above formula would give A=0, and thus the $\chi^{(2)}$ components would be zero. On the other hand, if a pixel contains two fibrils with the same alignment and weight w, but the same sign of β_{yyy}, the amplitude would be 2w (and depending on whether they were both positive or negative fibrils, A would be either positive or negative). Thus the amplitude A can be understood as a measure

of overall nonlinear response strength from that pixel, which when high means there is a net alignment of fibrils, and when low, indicates either no fibrils or a net misalignment. Thus, the equations for the effective single fibril from which we need to retrieve the effective angles become

$$\chi^{(2)}_{xxx} = A\sin\phi\cos\theta[-\sin^2\phi\cos^2\theta|\beta_{yyy}| + 3(\sin^2\phi\cos^2\theta - 1)|\beta_{yxx}|] \tag{21}$$

$$\chi^{(2)}_{xxy} = A\cos\phi\cos\theta[\sin^2\phi\cos^2\theta|\beta_{yyy}| - (3\sin^2\phi\cos^2\theta - 1)|\beta_{yxx}|] \tag{22}$$

$$\chi^{(2)}_{xyy} = A\sin\phi\cos\theta[-\cos^2\phi\cos^2\theta|\beta_{yyy}| + (3\cos^2\phi\cos^2\theta - 1)|\beta_{yxx}|] \tag{23}$$

$$\chi^{(2)}_{yyy} = A\cos\phi\cos\theta[\cos^2\phi\cos^2\theta|\beta_{yyy}| - 3(\cos^2\phi\cos^2\theta - 1)|\beta_{yxx}|] \tag{24}$$

given the four χ^2_{ijk} and $|\beta_{yyy}|$ and $|\beta_{yxx}|$, we need to apply these equations to find ϕ, θ, and A.

While in general such a complicated nonlinear system of equations would require a numerical approach, there do exist analytical solutions in our case. For example, by adding the first and third equations together and the second and fourth equations together we obtain

$$\chi^{(2)}_{xxx} + \chi^{(2)}_{xyy} = -A\sin\phi\cos\theta[\cos^2\theta|\beta_{yyy}| - (3\cos^2\theta - 4)|\beta_{yxx}|] \tag{25}$$

$$\chi^{(2)}_{xxy} + \chi^{(2)}_{yyy} = -A\cos\phi\cos\theta[\cos^2\theta|\beta_{yyy}| - (3\cos^2\theta - 4)|\beta_{yxx}|] \tag{26}$$

which gives

$$\tan\phi = -\frac{\chi^{(2)}_{xxx} + \chi^{(2)}_{xyy}}{\chi^{(2)}_{xxy} + \chi^{(2)}_{yyy}} \tag{27}$$

This will return a value of ϕ between $-\frac{\pi}{2}$ and $\frac{\pi}{2}$, and thus is incomplete. To get our final value of ϕ, we need to determine the sign of A. If its sign is negative, then we add π to ϕ. After this is done, we the adjust ϕ to be in the (top $(-\pi, \pi)$ by adding or subtracting 2π as appropriate.

Though in this work we only consider $\theta = 0$ as a first test, we can derive from Eqs. [21-24] expressions for $\cos^2\theta$. By dividing the first equation by the third equation, the re-arranging, we obtain

$$\cos^2\theta = \frac{|\beta_{yxx}|}{|\beta_{yyy}| - 3|\beta_{yxx}|}\frac{\chi^{(2)}_{xxx} - 3\chi^{(2)}_{xyy}}{\chi^{(2)}_{xyy}\cos^2\phi - \chi^{(2)}_{xxx}\sin^2\phi} \tag{28}$$

and by dividing the second equation by the fourth, and re-arranging, we obtain

$$\cos^2\theta = \frac{|\beta_{yxx}|}{|\beta_{yyy}| - 3|\beta_{yxx}|}\frac{\chi^{(2)}_{yyy} - 3\chi^{(2)}_{xxy}}{\chi^{(2)}_{xxy}\cos^2\phi - \chi^{(2)}_{yyy}\sin^2\phi} \tag{29}$$

even though our technique is designed to construct only the in-plane χ^2_{ijk} components (meaning, in components containing an x and/or y), we are able to derive an expression to retrieve information regarding the out-of-plane angle, θ, which gives the angle of the fibril with respect to the laser propagation axis, z.

The effective fibril amplitude A for each pixel can be calculated for each component by inverting [21-24], giving

$$A_{xxx} = \frac{\chi^{(2)}_{xxx}}{\sin\phi\cos\theta[-\sin^2\phi\cos^2\theta|\beta_{yyy}| + 3(\sin^2\phi\cos^2\theta - 1)|\beta_{yxx}|]} \tag{30}$$

$$A_{xxy} = \frac{\chi^{(2)}_{xxy}}{\cos\phi\cos\theta[\sin^2\phi\cos^2\theta|\beta_{yyy}| - (3\sin^2\phi\cos^2\theta - 1)|\beta_{yxx}|]} \tag{31}$$

$$A_{xyy} = \frac{\chi^{(2)}_{xyy}}{\sin\phi\cos\theta[-\cos^2\phi\cos^2\theta|\beta_{yyy}| + (3\cos^2\phi\cos^2\theta - 1)|\beta_{yxx}|]} \tag{32}$$

$$A_{yyy} = \frac{\chi^{(2)}_{yyy}}{\cos\phi\cos\theta[\cos^2\phi\cos^2\theta|\beta_{yyy}| - 3(\cos^2\phi\cos^2\theta - 1)|\beta_{yxx}|]} \tag{33}$$

While these should give the same value, we obtain a simpler formula by adding Eqs. [30-33] and re-arranging to obtain

$$A = \frac{\chi^{(2)}_{xxx} + \chi^{(2)}_{xxy} + \chi^{(2)}_{xyy} + \chi^{(2)}_{yyy}}{(\cos\phi - \sin\phi)\cos\theta[\cos^2\theta|\beta_{yyy}| - (3\cos^2\theta - 4)|\beta_{yxx}|]} \tag{34}$$

Which for the case of $\theta = 0$ becomes

$$\frac{\chi^{(2)}_{xxx} + \chi^{(2)}_{xxy} + \chi^{(2)}_{xyy} + \chi^{(2)}_{yyy}}{(\cos\phi - \sin\phi)(|\beta_{yyy}| + |\beta_{yxx}|)} \tag{35}$$

Applying this process to a simulated collagen sample it is possible to extract the effective angles. A methodology for retrieving the alignment of such a generated collagen sample from the laboratory frame components under the assumption that the azimuthal angle of each fibril +x is allowed to vary and the polar angle is restricted to zero.

3

Tensorial Ptychographic Iterative Engine

3.1 Generalized Model of tPIE

Ptychography is an iterative computational technique for imaging was developed to reconstruct both the complex-valued transmission function of an illuminated object as well as the magnitude and phase of the illuminating beam by using far-field diffraction patterns [52, 53, 54]. Ptychography was initially developed for imaging crystalline structure with electron microscopy in 1969 [55, 56]. It was applied experimentally for the first time only in 1994 due to the previous insufficiency in detector quality [57]. Since 1994 ptychography has undergone further revision and improvement, starting with the introduction of the Ptychographical Iterative Engine (PIE) in 2004 where multiple far-field diffractive images of different beam positions – rather than a single wide-field image – were used to reconstruct both magnitude and phase of the transmission function [37]. This is accomplished either with or without the use of a collecting lens. The key to the reconstruction is that the object must be "oversampled", that is, there must significant overlap in the illuminated areas of the object from shot to shot. Using this technique,

the transmission function can be reconstructed with a resolution down to the diffraction limit of the scattered light, which is typically much smaller than the spot size of the input beam. Further developments to the PIE include the extended ptychographic Iterative Engine (ePIE) which allows for the simultaneous recovery of both the transmission function of the object and the phase and magnitude of the input beam itself, and consequently delivers a much faster and much improved reconstruction – even when a model for the input beam is unavailable [54]. The vectorial Ptychographic Iterative Engine (vPIE) further extended the PIE for the study of birefringence and diattenuation of anisotropic specimens, by using multiple polarized input beams [40, 41].

Ptychography has seen application in 2D materials [58, 59], Nonlinear Imaging [38], Optical Metrology [60, 61], 3D imaging [62, 63] and Biomedical Imaging [64, 65]. There is however currently no literature for the application of ptychography to biomedical samples using nonlinear optical microscopy.

The purpose of this work is to develop and test a methodology for ptychographic reconstruction to study the organization of a sample of fibrillar collagen using Second Harmonic Generation (SHG) imaging. We develop a new approach for ptychographic reconstruction that is a replacement for (and improvement of) both polarization SHG (pSHG) – which can return alignment information about a sample at the cost of requiring a large number exposures with repetition for each polarization state [32] – and interferometric SHG (iSHG) – which can retrieve the phase of a sample with the added requirement of a stable reference beam, and a large number of exposures for each phase [48]. This new imaging methodology which we will refer to as the "tensorial Ptychographical Iterative Engine" (tPIE) will allow for the simultaneous reconstruction of multiple components of the nonlinear optical susceptibility tensor which can be analyzed to retrieve information about the sample organization. We show that for a collagen sample with fibrils of differing alignment and polarity, we are able to retrieve both the alignment and the relative polarity, with far fewer laser exposures than either I-SHG or P-SHG. This occurs since we are not limited to a confocal geometry, but can obtain resolution down to the diffraction limit at the SHG wavelength with much larger laser spot sizes. In order to perform tensorial reconstruction for nonlinear optical microscopy, the basic model of ptychography needs to be reformatted and extended. The building blocks of Ptychography are the "probe" – which is typically related to the input beam –the "object" – which is typically related to the local optical response of the sample being imaged – and the "exit field" – which is typically the product of the object and probe.

By applying ptychography to nonlinear optical microscopy, our goal is to reconstruct the complex-valued nonlinear optical susceptibility tensor of the sample, which includes phase information. We thus take the nonlinear optical susceptibility of interest to be the "object", which for an nth order perturbative nonlinear process is written as

$$Object: \quad \chi^{(n)}_{i,j_1,\ldots,j_n}(\vec{r}) \tag{36}$$

We take the "exit field" to be the nonlinear field generated at the sample upon illumination, that is, the induced nonlinear polarization. For an nth order perturbative nonlinear process, this is written as

$$ExitField: \quad \vec{P}(\vec{r}) = \overset{\leftrightarrow}{\chi}^{(n)}(\vec{r})\vec{E}^n(\vec{r}-\vec{r}_m) \tag{37}$$

where the input field $\vec{E}^n(\vec{r}-\vec{r}_m)$ can in general be centered at any location $\vec{r}_m$ within the sample; we write this dependence explicitly here as it simplifies the notation when we later consider illuminating the sample at multiple locations. This multiple illumination is illustrated in fig 4. Rather than take the probe to be the input field itself, from the definition of the exit field we see that it makes more sense for the probe to be defined as

$$Probe: \quad \vec{E}^n(\vec{r}-\vec{r}_m) \tag{38}$$

Which in the work the input field is assumed to arise from a single laser beam, though this could be easily generalized. We fix the laser propagation axis to be in the z-direction, and consider the input beam to have a fixed transverse spatial profile that is known, and to be linearly polarized in any direction in the xy-plane. It will prove convenient to write the input field as

$$\vec{E}^n(\vec{r}-\vec{r}_m) = \hat{h}(\gamma)E(\vec{r}-\vec{r}_m) \tag{39}$$

where

$$\hat{h}(\gamma) = \cos\gamma\hat{x} + \sin\gamma\hat{y} \tag{40}$$

is a unit vector in the xy-plane that defines the direction of the input field's polarization, which as defined will be an angle γ counterclockwise from the x axis. $\hat{x}, \hat{y}$ are unit vectors in the positive x and y directions, respectively. For clarity, this is illustrated in fig 5 In tensor component notation, the tensorial probe components are

$$[\vec{E}^n(\vec{r}-\vec{r}_m)]_{j_1,j_2,\ldots,j_n} = h_{j_1}(\gamma)h_{j_2}(\gamma)\ldots h_{j_n}(\gamma)(E(\vec{r}-\vec{r}_m))^n \tag{41}$$

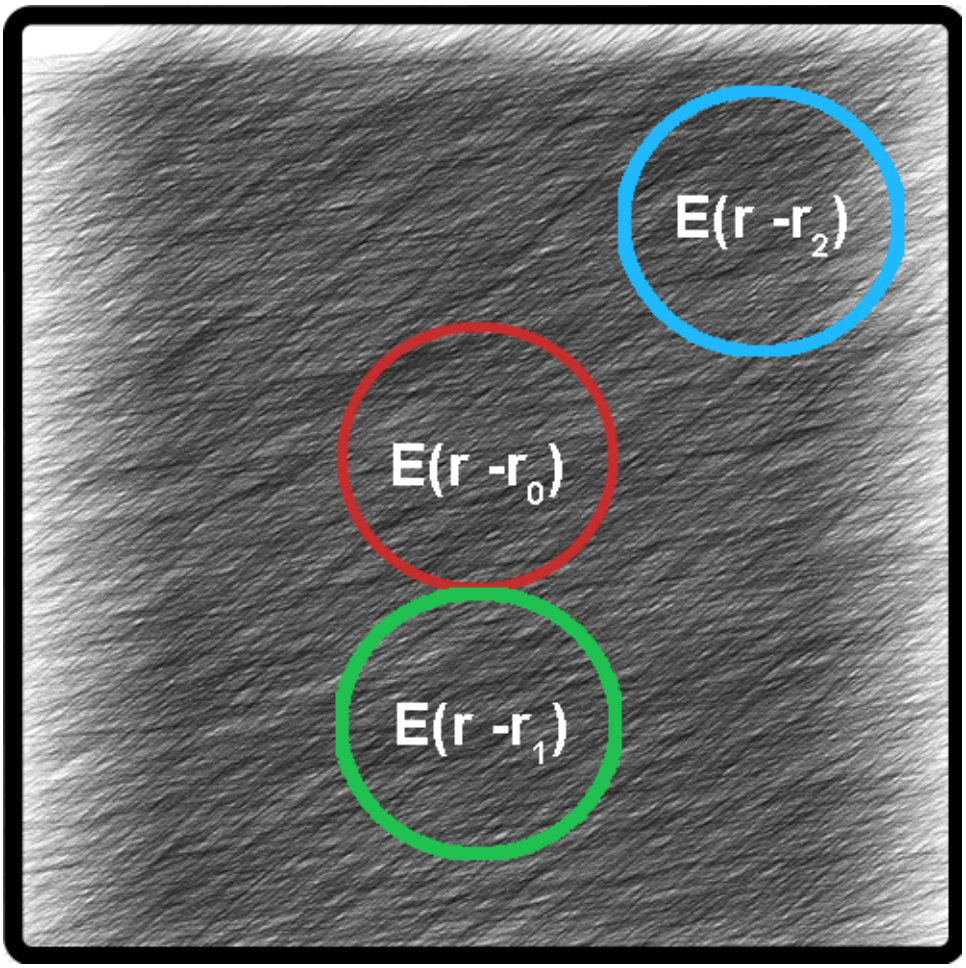

Figure 4: The position of the input beam is varied to allow imaging of the entire sample.

and the i-th component of the induced polarization vector is

$$P_i(\vec{r}) = \chi^{(n)}_{i,j_1,j_2,\ldots,j_n}(\vec{r})h_{j_1}(\gamma)h_{j_2}(\gamma)...h_{j_n}(\gamma)(E(\vec{r}-\vec{r}_m))^n \equiv \psi^{(m)}_i(\vec{r},\gamma) \tag{42}$$

In the language of Ptychography the induced polarization is equivalent to the exit field, which in order to be consistent with the ptychography literature we will refer to from here on as, ψ. The superscript m refers to the position of the laser beam in the sample (the measurement position), and the angle γ is also explicitly included, as it denotes the polarization of the input beam used for that measurement. Initially, the exit field is a product of our guessed object and known probe.

For this work, we consider the object to be restricted to a 2D plane which is like considering a sample thinner than the Rayleigh range of the illuminating laser beam.

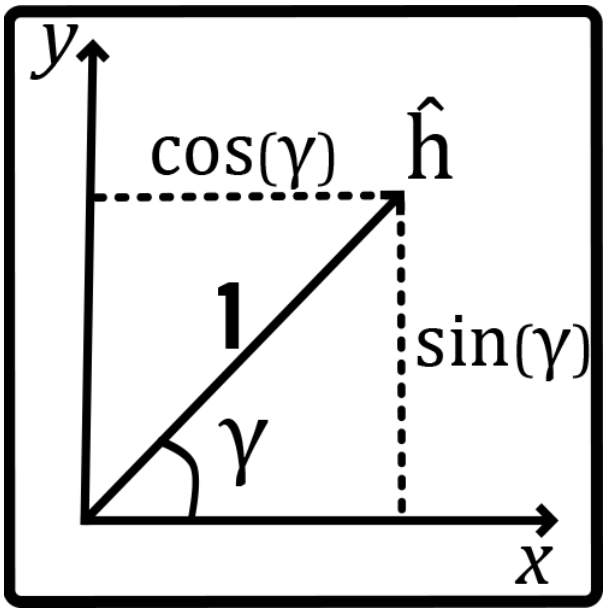

Figure 5: The unit vector that handles the linear polarization of the input beam is described by applying the polarization angle trigonometrically

Taking the 2D object to be at $= z_0$, the position vectors are then

$$\vec{r} = x\hat{x} + y\hat{y} + z_0\hat{z} \tag{43}$$

$$\vec{r}_m = x_m\hat{x} + y_m\hat{y} + z_0\hat{z} \tag{44}$$

$$\vec{r} - \vec{r}_m = (x - x_m)\hat{x} + (y - y_m)\hat{y} + 0\hat{z} \tag{45}$$

$$\tag{46}$$

and the exit field becomes

$$\psi_i^{(m)}(x, y, \gamma) = \chi^{(n)}_{i,j_1,j_2,...,j_n}(x, y)h_{j_1}(\gamma)h_{j_2}(\gamma)...h_{j_n}(\gamma)(E(x - x_m, y - y_m))^n \tag{47}$$

The process of obtaining the exit-field is summarized in fig 6. The schematic denotes the location of the beam, object, and exit-field in the theoretical optical system. Now that we have an expression for the exit-field we require its far-field equivalent since the data used in our algorithm consists of "experimentally" measured far-field intensity images – in this work we will use numerical experiments to generate the diffractive images. In essence, we make a guess for an object, which produces a guess for the exit-field, from which we obtain a guessed far-field.

Assuming the guessed exit field propagates through free space to the detector location,

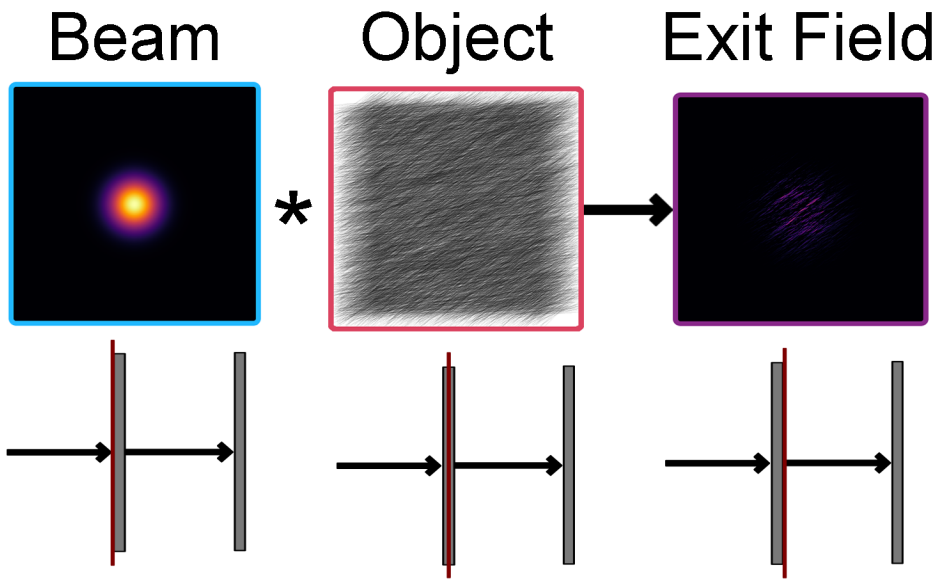

Figure 6: Schematic diagram for exit-field formation (bottom) with demonstrative images (top). Arrows denote the direction of field propagation with the first gray box on the left denoting the exit-field region and the following gray box on the right denoting the far-field. A red line appears to indicate the position of the beam, object, and exit-field at each respective step of the diagram.

the guessed far field given by [66]

$$k^2 \frac{\exp(ikR)}{4\pi R} \int\int \psi_i^{(m)}(x, y, \gamma) \exp(iq_x x) \exp(iq_y y) dx dy \tag{48}$$

Where $k = \omega c$, ω is the nonlinear frequency of interest, c is the speed of light, R is the distance to the far-field, and $\vec{q} = k\frac{X}{R}\hat{x} + k\frac{Y}{R}\hat{y}$, where X and Y are the transverse spatial coordinates in the image plane. Without loss of generality, we neglect the overall amplitude and phase factor outside the integral, and set the guessed far-field as

$$\Psi_i^{(m)}(q_x, q_y, \gamma) = \mathcal{F}\{\psi_i^{(m)}(x, y, \gamma)\} \tag{49}$$

Where $\mathcal{F}$ denotes the 2D Fourier Transform operation over x,y space.

The experimentally measured far-field intensity patterns are recorded on a CCD after first passing through a linear polarizer, which will be at an angle ν with respect to the x-axis. Thus, the fields that are measured result from a projection of $\Psi_i^{(m)}(q_x, q_y, \gamma)$ along the unit vector $\hat{h}(\nu)$, where $\hat{h}$ is as previously defined, but this time as a function of the output polarizer angle ν. The quantity resulting from this projection will be a complex

scalar quantity, and represents the field (in the direction of $\hat{h}(\nu)$) that reaches the CCD camera as position $\vec{q}$. We refer to this as the guessed scalar far-field, ξ, given by

$$\xi^{(m)}(q_x, q_y y, \gamma, \nu) = \hat{h}(\nu)\vec{\Psi}^{(m)}(q_x, q_y, \gamma) \equiv h_i(\nu)\Psi_i^{(m)}(q_x, q_y, \gamma) \tag{50}$$

where summation over i is implied. The guessed scalar far-field is written such that it has an explicit dependence on the far-field coordinates $\vec{q}$, the location of the input beam within the sample (denoted by the superscript m), the polarization angle of the input beam γ, as well as the output polarizer angle ν; this allows us to keep track of all of the relevant information about the current measurement for each polarization state in a form that can be directly compared to the measurement data.

Now we outline an approach for updating all the relevant components of $\overleftrightarrow{\chi}^{(n)}(\vec{r})$ over all the $\vec{r}$ in the sample. In essence, we will combine our "experimental" measurement data with our guessed far-field to produce a hybrid far-field To do this, we need to use the intensity diffraction patterns, $I^{(m)}(\vec{q}_l, \gamma, \nu)$, measured on a CCD camera where there would be a separate measurement for each input beam polarization angle γ and each output polarizer angle ν at every probe location (labeled by superscript m); the $\vec{q}_l$ denotes the discrete pixel positions on the CCD camera. We will pull the phase information from the guessed scalar far-field $\xi^{(m)}(q_x, q_y, \gamma, \nu)$ and the known magnitude information from the experimental data $I^{(m)}(\vec{q}, \gamma, \nu)$, in order to create a hybrid far-field that is used to update our guesses for $\overleftrightarrow{\chi}^{(n)}(\vec{r})$. We begin by assuming that the deviation between the square root of the measured intensity and the absolute value of the guesses scalar far-field $\xi^{(m)}(q_x, q_y y, \gamma, \nu)$ follows a Gaussian distribution for each probe position $\vec{r}_m$, each CCD pixel position $\vec{q}_l$, and each angle γ and ν. We follow the work for scalar linear ptychography presented in [67], where they account for the potential presence of photon noise in the measurement data. We take this deviation to be

$$\epsilon^{(m)}(\vec{q}_l, \gamma, \nu) = \sqrt{I^{(m)}(\vec{q}_l, \gamma, \nu)} - |\xi^{(m)}(\vec{q}_l, \gamma, \nu)| \tag{51}$$

Which we assume is Gaussian distributed with constant variance σ^2, with all variates statistically independent. Under this condition the probability density function (PDF) is

$$f = \prod_{\vec{q}_l} \prod_{m} \prod_{\gamma,\nu} \frac{1}{\sqrt{2\pi\sigma^2}} \exp[-\frac{1}{2}(\frac{\sqrt{I^{(m)}(\vec{q}_l, \gamma, \nu)} - |\xi^{(m)}(\vec{q}_l, \gamma, \nu)|}{\sigma})^2] \tag{52}$$

The maximum likelihood principle is now applied, where the maximum likelihood estimator for the object is the quantity that maximizes Eq. 52. In order to compute a

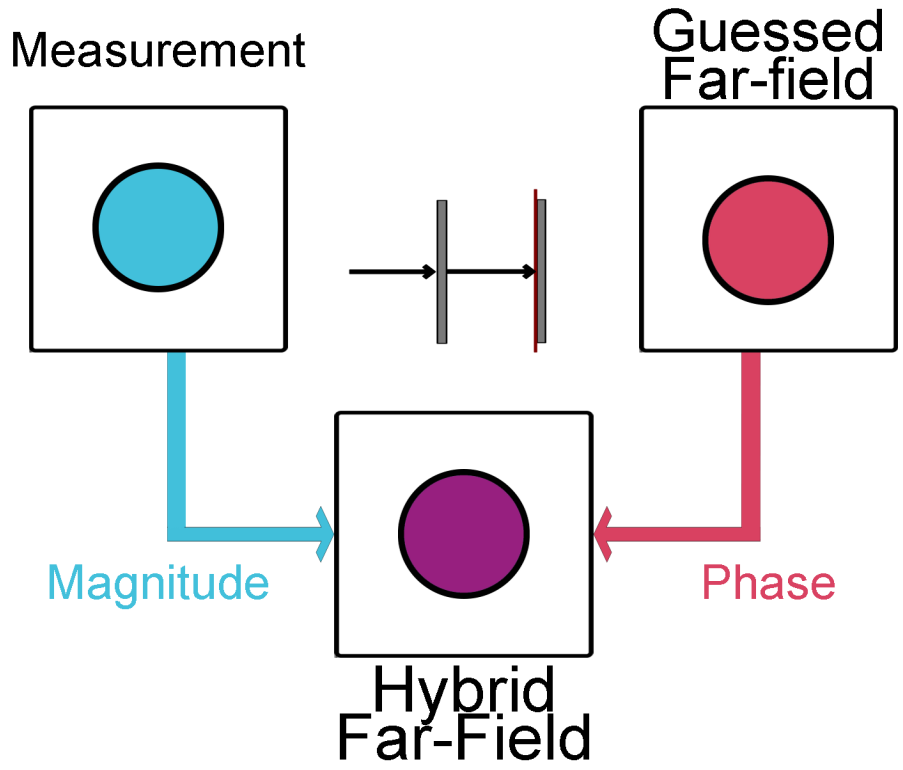

Figure 7: Diagram depicting the combination of guessed and measured far-field information to obtain a hybrid far-field

maximum for this quantity we aim to minimize the negative of the log likelihood for a given probe position m

$$\mathcal{L}^{(m)} = \sum_{\vec{q}_l} \sum_{\gamma,\nu} |\sqrt{I^{(m)}(\vec{q}_l,\gamma,\nu)} - |\xi^{(m)}(\vec{q}_l,\gamma,\nu)||^2 \tag{53}$$

To minimize the negative log likelihood, we must take the gradient of $\mathcal{L}^{(m)}$ with respect to the object at one position in sample space. Following [67] we obtain

$$\frac{\partial \mathcal{L}^{(m)}}{\partial \chi^{(n)}_{i,j_1,j_2,\ldots,j_n}(x,y)} = -2 \sum_{\gamma,\nu} h_i(\nu) h_{j_1}(\gamma) h_{j_2}(\gamma) \ldots h_{j_n}(\gamma) (E^*(\vec{r} - \vec{r}_m))^2 \Delta\psi^{(m)}(x,y,\gamma,\nu) \tag{54}$$

where

$$\Delta\psi^{(m)}(x,y,\gamma,\nu) = \mathcal{F}^{-1}\{\frac{\sqrt{I^{(m)}(\vec{q}_l,\gamma,\nu)}}{|\xi^{(m)}(\vec{q}_l,\gamma,\nu)|}\xi^{(m)}(\vec{q}_l,\gamma,\nu) - \xi^{(m)}(\vec{q}_l,\gamma,\nu)\} \tag{55}$$

We see that the gradient depends on the difference between a hybrid scalar far-field

$$\frac{\sqrt{I^{(m)}(\vec{q}_l,\gamma,\nu)}}{|\xi^{(m)}(\vec{q}_l,\gamma,\nu)|}\xi^{(m)}(\vec{q}_l,\gamma,\nu) \tag{56}$$

with the phase of $\xi^{(m)}(\vec{q}_l, \gamma, \nu)$ and the amplitude of $\sqrt{I^{(m)}(\vec{q}_l, \gamma, \nu)}$, and our original guessed scalar far-field $\xi^{(m)}(\vec{q}_l, \gamma, \nu)$.

Now that we have the derivative of the negative log likelihood function with respect to the object, we use it in a gradient descent optimization approach to obtain update equations for each component and for each position (x,y) in the sample space. They are thus given by

$$\chi^{(n)updated}_{i,j_1,j_2,\ldots,j_n}(x,y) = \chi^{(n)}_{i,j_1,j_2,\ldots,j_n}(x,y) + \beta \frac{\partial \mathcal{L}^{(m)}}{\partial \chi^{(n)}_{i,j_1,j_2,\ldots,j_n}(x,y)} \tag{57}$$

where β is a free parameter that determines the speed of the gradient descent. This update equation forms the heart of the tensorial Ptychographical Iterative Engine

3.2 tPIE for Second Harmonic Generation Imaging

In this work, we apply tPIE to second harmonic generation (SHG) imaging. The object is the second order nonlinear susceptibility tensor $\chi^{(2)}_{ijk}(x,y)$, and the exit field is

$$\psi^{(m)}_i(x,y,\gamma) = \chi^{(n)}_{ijk}(x,y) h_j(\gamma) h_k(\gamma) (E(x - x_m, y - y_m))^2 \tag{58}$$

Where the input beam $E(x - x_m, y - y_m)$ is assumed to have a Gaussian transverse profile, propagate in the z-direction, and be linearly polarized with angle γ with respect to the x-axis. The only $\chi^{(2)}_{ijk}$ we have access to with this input beam are those with i,j,k = x or y only.

In order for our ptychographic reconstruction technique to reconstruct these components with the correct relative phase, it is necessary for the data set to include redundant measurements not only with regards to probe position as discussed above, but also with regards to polarization of the input beam. If we were to choose only x and y polarized beams by setting $\gamma = 0$ and 90^o , for example, we find that the reconstruction fails. Thus, in addition to measurements with x and y polarized beams, we also need a measurement that overlaps the information in these two measurement sets. Thus, we need to create a third measurement set at another angle [40], and we choose this angle to be $\gamma = 45^o$.

The components of the guessed exit-fields then can be written explicitly as

$$\psi_x^{(m)}(x,y,0) = \chi_{xxx}^{(2)}(x,y)(E(x-x_m,y-y_m))^2 \tag{59}$$

$$\psi_y^{(m)}(x,y,0) = \chi_{yxx}^{(2)}(x,y)(E(x-x_m,y-y_m))^2 \tag{60}$$

$$\psi_x^{(m)}(x,y,45) = \frac{1}{2}[\chi_{xxx}^{(2)}(x,y) + \chi_{xxy}^{(2)}(x,y) + \chi_{xyx}^{(2)}(x,y) + \chi_{xyy}^{(2)}(x,y)](E(x-x_m,y-y_m))^2 \tag{61}$$

$$\psi_y^{(m)}(x,y,45) = \frac{1}{2}[\chi_{yxx}^{(2)}(x,y) + \chi_{yxy}^{(2)}(x,y) + \chi_{yyx}^{(2)}(x,y) + \chi_{yyy}^{(2)}(x,y)](E(x-x_m,y-y_m))^2 \tag{62}$$

$$\psi_x^{(m)}(x,y,90) = \chi_{xyy}^{(2)}(x,y)(E(x-x_m,y-y_m))^2 \tag{63}$$

$$\psi_y^{(m)}(x,y,90) = \chi_{yyy}^{(2)}(x,y)(E(x-x_m,y-y_m))^2 \tag{64}$$

The guessed scalar far-fields (after applying the output polarizer angle ν, which we also take to be $0^o, 45^o, 90^o$, are then

$$\xi^{(m)}(q_x,q_y,0,0) = \mathcal{F}\{\psi_x^{(m)}(x,y,0)\} \tag{65}$$

$$\xi^{(m)}(q_x,q_y,0,45) = \frac{1}{\sqrt{2}}\mathcal{F}\{\psi_x^{(m)}(x,y,0) + \psi_y^{(m)}(x,y,0)\} \tag{66}$$

$$\xi^{(m)}(q_x,q_y,0,90) = \mathcal{F}\{\psi_y^{(m)}(x,y,0)\} \tag{67}$$

$$\xi^{(m)}(q_x,q_y,45,0) = \mathcal{F}\{\psi_x^{(m)}(x,y,45)\} \tag{68}$$

$$\xi^{(m)}(q_x,q_y,45,45) = \frac{1}{\sqrt{2}}\mathcal{F}\{\psi_x^{(m)}(x,y,45) + \psi_y^{(m)}(x,y,45)\} \tag{69}$$

$$\xi^{(m)}(q_x,q_y,45,90) = \mathcal{F}\{\psi_y^{(m)}(x,y,45)\} \tag{70}$$

$$\xi^{(m)}(q_x,q_y,90,0) = \mathcal{F}\{\psi_x^{(m)}(x,y,90)\} \tag{71}$$

$$\xi^{(m)}(q_x,q_y,90,45) = \frac{1}{\sqrt{2}}\mathcal{F}\{\psi_x^{(m)}(x,y,90) + \psi_y^{(m)}(x,y,90)\} \tag{72}$$

$$\xi^{(m)}(q_x,q_y,90,90) = \mathcal{F}\{\psi_y^{(m)}(x,y,90)\} \tag{73}$$

These correspond to the nine diffractive patterns that must be measured for each probe position (x_m, y_m). Recalling that $\Delta\psi^{(m)}(x,y,\gamma,\nu)$ is defined in eq 55 as the inverse Fourier transform of the hybrid scalar field minus the guessed scalar far-field, and applying eq 57 which gives the update equation for the nonlinear susceptibility, the update

equations for the relevant components of $\overleftrightarrow{\chi}^{(2)}$ become

$$\chi^{(2),updated}_{xxx}(x,y) = \chi^{(2)}_{xxx}(x,y) + \beta(E^*(x-x_m, y-y_m))^2 \tag{74}$$
$$\times(\Delta\psi^{(m)}(x,y,0,0) + \frac{\Delta\psi^{(m)}(x,y,0,45)}{\sqrt{2}} + \frac{\Delta\psi^{(m)}(x,y,45,0)}{2} + \frac{\Delta\psi^{(m)}(x,y,45,45)}{2\sqrt{2}})$$
$$\chi^{(2),updated}_{xyy}(x,y) = \chi^{(2)}_{xyy}(x,y) + \beta(E^*(x-x_m, y-y_m))^2 \tag{75}$$
$$\times(\frac{\Delta\psi^{(m)}(x,y,45,0)}{2} + \frac{\Delta\psi^{(m)}(x,y,45,45)}{2\sqrt{2}} + \Delta\psi^{(m)}(x,y,90,0) + \frac{\Delta\psi^{(m)}(x,y,90,45)}{\sqrt{2}})$$
$$\chi^{(2),updated}_{xxy}(x,y) = \chi^{(2)}_{xxy}(x,y) + \beta(E^*(x-x_m, y-y_m))^2 \tag{76}$$
$$\times(\frac{\Delta\psi^{(m)}(x,y,45,0)}{2} + \frac{\Delta\psi^{(m)}(x,y,45,45)}{2\sqrt{2}})$$
$$\chi^{(2),updated}_{yyy}(x,y) = \chi^{(2)}_{yyy}(x,y) + \beta(E^*(x-x_m, y-y_m))^2 \tag{77}$$
$$\times(\frac{\Delta\psi^{(m)}(x,y,45,45)}{2\sqrt{2}} + \frac{\Delta\psi^{(m)}(x,y,45,90)}{2} + \frac{\Delta\psi^{(m)}(x,y,90,45)}{\sqrt{2}} + \Delta\psi^{(m)}(x,y,90,90))$$

Earlier it was mentioned that due to Where the profile and propagation of the input beam only components with x and y indices are accessible, this however leaves 8 remaining components of the $\overleftrightarrow{\chi}^{(2)}$ tensor of which only six are considered in the update equations and due to Kleinman symmetry only four are independent $\chi^{(2)}_{xxx}$, $\chi^{(2)}_{xxy}$, $\chi^{(2)}_{xyy}$, and $\chi^{(2)}_{yyy}$. Due to symmetry components with a permutation of indices are equivalent which means the following non-zero components are independent $\chi^{(2)}_{xxy} = \chi^{(2)}_{xyx} = \chi^{(2)}_{yxx}$ and $\chi^{(2)}_{xyy} = \chi^{(2)}_{yyx} = \chi^{(2)}_{yxy}$.

3.3 Creating Numerical Measurements

While the model for the tPIE is well described by the update equation, we now describe in this section how we create numerical "measurement data" that will be used in tPIE for our reconstruction. The generation of numerical collagen fibrillar samples was described in the previous chapter. Here we describe how we take our numerical samples and produce the measurement data, that is, the diffraction patterns $I^{(m)}(\vec{q}_l, \gamma, \nu)$.

The simulation of creating measurements from a simulated sample occurs in three steps, (1) the calculation of the exit field, (2) shifting the exit field to the far-field,

and finally (3) applying diffraction. This measurement simulation is repeated for all permutations of polarization angles for each measurement position. The exit field for each measurement is calculated by applying Eqs. [65 - 73] above. After the exit-field has been calculated for a given measurement, a 2D discrete Fourier transform (DFT) is applied to shift into the far-field where the absolute value squared is retained.

Finally the numerical aperture (NA) of the detection apparatus is applied to the far-field diffraction pattern, by setting to zero any region of the far-field image that is beyond the numerical aperture angle. The Numerical Aperture (NA) defines the light gathering ability of an objective (or in the case of Ptychography a CCD camera). It directly relates to the angle of the cone formed between a point on the sample and the collector lens (or CCD camera), defined by $NA = n\sin(\theta)$ where n refers to the refractive index of the medium between the collector and the sample, which in our case we take to be air [68]. To simulate far-field diffraction using the NA the wavenumber for the SHG signal

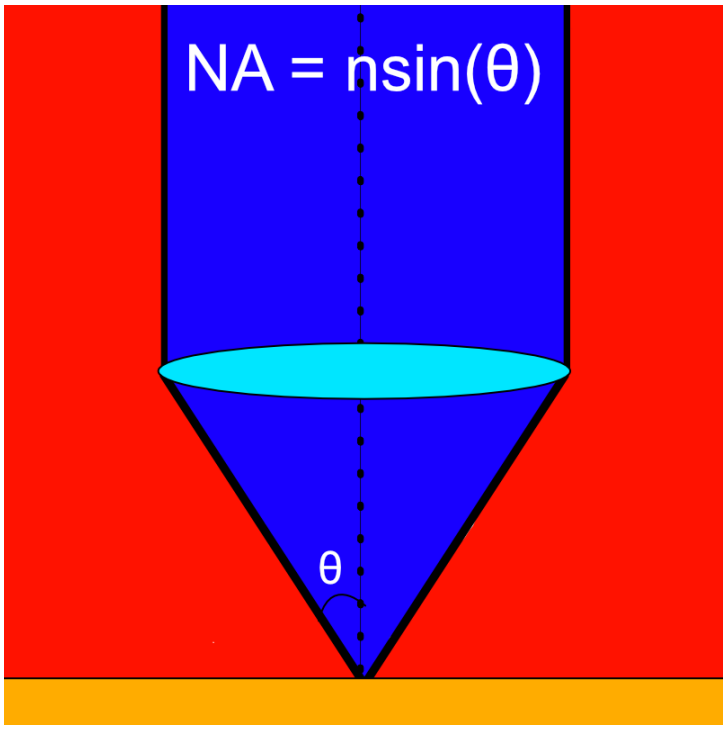

Figure 8: Diagram of Numerical Aperture depicting the cone of light gathered from a specimen (orange) by a collection lens or CCD camera (cyan) area colored in blue denotes light that is successfully collected and red denotes information that is not collected by a microscope.

$k = \frac{2\pi}{\lambda}$. The wavevector components in the x and y directions are calculated according

to

$$k_y = \begin{cases} 2\frac{m\pi}{d_y R} & m < \frac{R}{2} \\ -2\frac{\pi R - \pi m}{d_y R} & otherwise \end{cases} \tag{78}$$

$$k_x = \begin{cases} 2\frac{n\pi}{d_x R} & n < \frac{R}{2} \\ -2\frac{\pi R - \pi n}{d_x R} & otherwise \end{cases} \tag{79}$$

where m and n refer to the indices of the pixels on the CCD camera in the y and x direction respectively, d_y and d_x refer to the size of a pixel on the CCD camera in the y and x direction respectively, and R refers to the total number of pixels in either direction on the CCD camera. The expected wavenumber is then compared to these explicit wavenumbers by $NA^2k^2 < k_x^2 + k_y^2$ and in the case that this comparison is true for a pixel coordinate then that pixel is set to zero otherwise the pixel is left alone. What results is a measurement with non-zero pixels restricted to those that would be illuminated with the defined NA value. Finally the resulting measurements are stored for access during ptychographic reconstruction.

4

Retrieving the Orientation of Collagen Fibrils with tPIE

In this chapter we demonstrate the results of our numerical collagen sample generation, described in chapter 2, in addition to the characterization of this numerical sample. We then demonstrate how we use numerical diffraction to create a set of measurements using the numerically generated sample. We apply these numerically generated measurements to the ptychography model outlined in chapter 3 and compare the reconstruction to the numerical sample. Finally using only the reconstructed components of the $\chi^{(2)}$ tensor we retrieve information about sample alignment and orientation and compare these results to the information retrieved from the numerical sample.

4.1 Collagen Sample Generation

The first step is to create and place fibrils into a sample. In order to generate a collagen sample using the methodology outlined in chapter 2, it is necessary to define the parameters of the sample, specifically how many collagen fibrils there will be, the total size of the sample, the range of possible sizes of each fibril, the f-ratio, and the range of angles

that each fibril can be rotated. We used fig 2 from chapter 2 as our fibril arrangement, which corresponds to 30,000 fibrils.

The parameters chosen for this project aim to create a realistic sample of collagen fibrils that are oriented such that they form two regions with net alignment, as well as a mixed alignment region. In order to accomplish this each fibril was placed in a simulation domain of size $51.2\mu m^2$ where each fibril has length $10\mu m$ and radius $0.055\mu m$. Each fibril was disallowed from rotating out of plane by restricting the polar angle, θ, to zero, the in-plane rotation however was allowed by uniformly sampling the azimuthal angle, ϕ, within the range $[0, \pi/4]$. For some of the fibrils, π was added to ϕ, indicating a different orientation, and thus a π phase shift in the $\chi^{(2)}$ from this fibril. This was controlled with an f-ratio that varies from 0.4 on one side to 0.6 on the opposite side with a value of 0.5 in the middle indicating a roughly equal number of positive and negative polarity, resulting in a sample with a central region with no general alignment, and two regions of opposite polarity.

The second step in generating a collagen sample is to calculate the numerical values of $\chi^{(2)}$ from the fibrils in the sample. A set of laboratory frame $\chi^{(2)}$ images are created from the placed fibrils as described in chapter 2.1, which with a resolution of 512×512 square cells each with a size of $0.1\mu m^2$; for convenience, the number of cells was chosen to match the number of detector pixels in our numerical CCD camera measurements.

The generated sample is obtained as a set of text files containing the real and imaginary parts for each relevant component of $\chi^{(2)}$. In order to maintain consistency throughout, all figures in this work are presented as in fig 9 with the components displayed in a grid with the top four plots the magnitude, and the bottom four plots the phase. For each 2×2 set, the top left entry depicts $\chi^{(2)}_{xxx}$ with $\chi^{(2)}_{xxy}$, on the top right, $\chi^{(2)}_{xyy}$ on the bottom left, and $\chi^{(2)}_{yyy}$ on the bottom right. To retain comparability between all figures, the scaling of the magnitude in all figures is the same for all components. This is set according the maximum and minimum value chosen with respect to all the components, corresponding to 1 and 0 on the color bar respectively. The phase of each component, similarly lines up with expectation as fibrils polarized in opposite directions should correspond with angles out of phase with each other, this is exactly what is shown in the phase images; three regions of phase mixing a region with predominant phase of π, a region of mixed phase angles, and a region of predominate $0/2\pi$ phase angles.

The final step is to retrieve the angles of a generated sample using the model presented in chapter 2.2. Before moving on, we would like to test our angle retrieval algorithm by

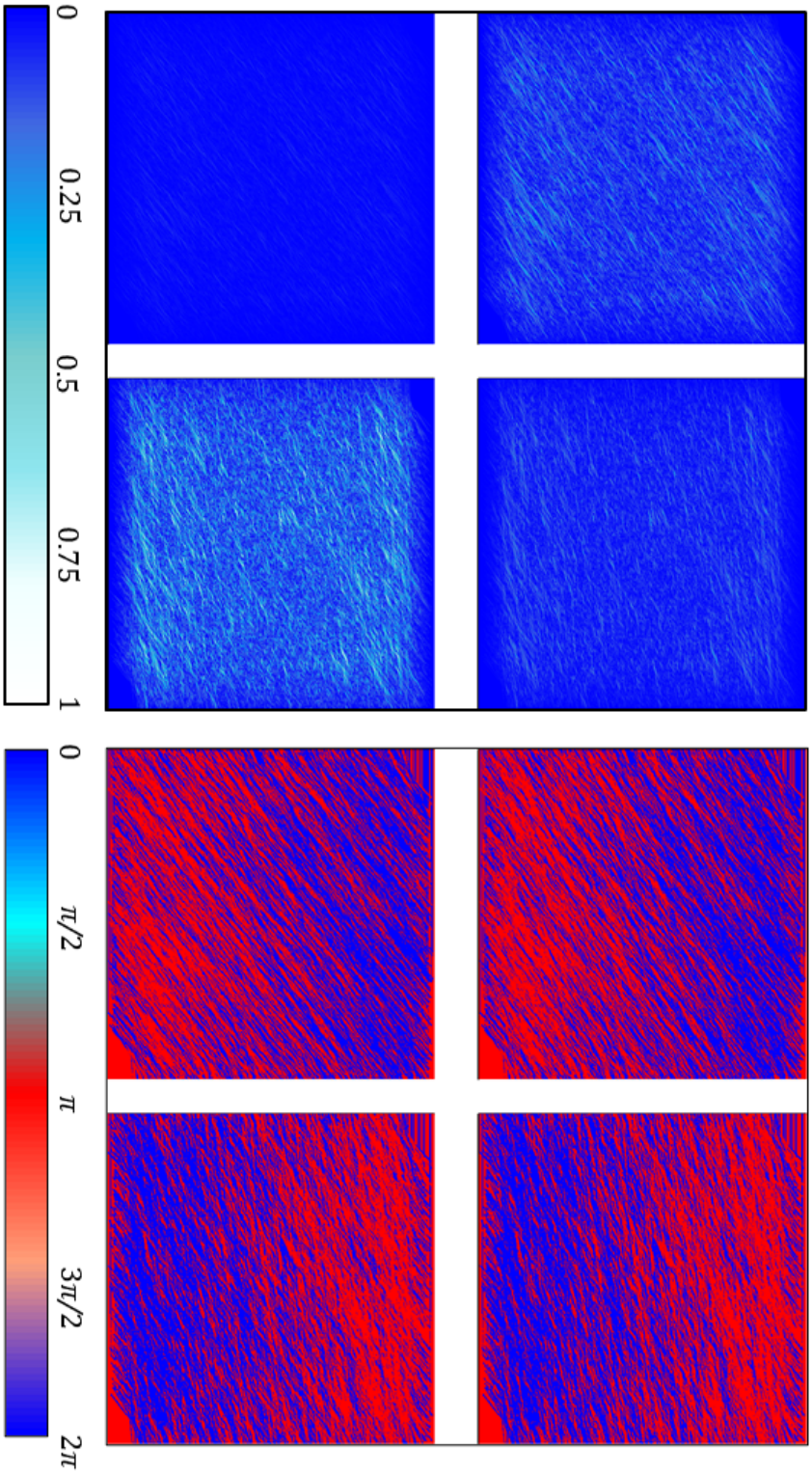

Figure 9: Both the phase (bottom) and the magnitude (top) can be visualized from the computationally generated collagen sample. The scaling of the magnitude images is uniform across all components and the phase components are all scaled from 0 to 2π with periodic coloring. The components are laid out as χ^2_{xxx} on the top left, χ^2_{xxy} on the top right, χ^2_{xyy} on the bottom left, and χ^2_{yyy} on the bottom right

applying it to our rasterized $\overleftrightarrow{\chi}^{(2)}$ tensor components. Recall with this method that we aim to retrieve an average angle associated with each pixel or a sample image, where we do this by considering that each pixel contains a single effective collagen fibril, in essence combining the angles of all overlaid real fibrils into one retrievable angle. As we have placed the fibrils such that they all lie in the xy plane, then the only angle to retrieve is the in-plane angle, ϕ.

In fig 10(top), we show a heat map of the ϕ angle retrieved from our rasterized $\chi^{(2)}$ samples.

Similar to the phase images, the heat-map of the azimuthal angle is colored to denote the angle of an effective fibril where the color range varies from $-\pi$ to π where fibrils with an angle of $-\pi$ are aligned in the opposite direction of a fibril with an angle of π, fibrils angled along zero represent an effective fibril constructed from fibrils aligned opposite to one another creating an effective fibril aligned perpendicular to those colored red or blue. In this image it is shown that the angle retrieval is able to accurately depict the regions of alignment where the top region is positively aligned while the bottom region is aligned negatively with the center region possessing no general alignment. In addition to the heat-map of azimuthal angles we also produce a heat-map of effective fibril amplitudes which can be used to determine the overall strength of the nonlinear response from a given effective fibril this is shown in figure 10(bottom).

In addition to the heat-maps of effective fibril orientation and amplitude, it is instructive to count the total number of occurrences for each angle in the sample of effective fibrils to create a histogram illustrating the most common alignment angles in a sample. This is plotted in fig 11 for both rasterized (top) and unrasterized (bottom) samples. It is worth noting that after rasterization while the distribution retains its bi-modal structure the two alignment regions form normal distributions, this can be attributed to the central limit theorem as the process of rasterization requires that uniformly generated random numbers be added together to account for overlap. The post-raster distribution serves as a best case scenario for a distribution of azimuthal angles retrieved from a set of rasterized $\chi^{(2)}$ samples reconstructed using ptychography as it is not possible to reconstruct the true distribution of fibril alignment due to overlap and rasterization.

The combination of each effective fibril's azimuthal angle ϕ and the histogram of the distribution of ϕ allow us to construct a 3D render of the "effective sample" where the "effective fibril" contained in each pixel is drawn in the image centered on that pixel, rotated according to its effective angle ϕ, and depicted with a length scaled according

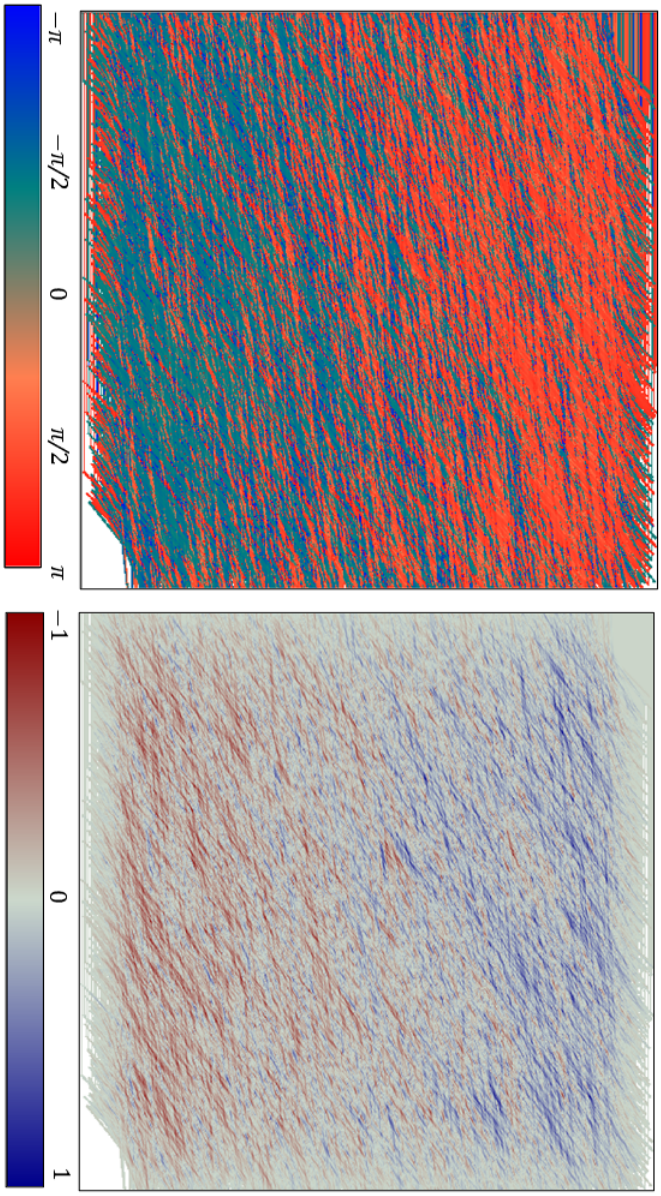

Figure 10: A map of azimuthal angles (top) and an amplitude map (bottom) for effective fibrils can be retrieved from rasterized $\chi^{(2)}$ samples and used to analyze the structure of a collagen sample as well as the nonlinear response of the sample.

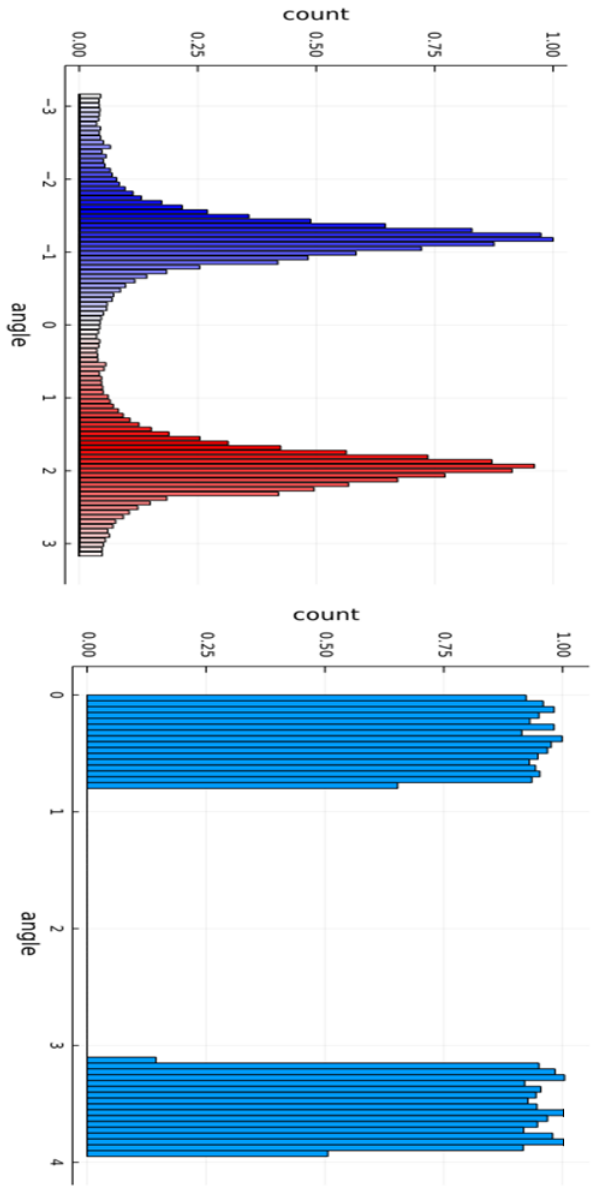

Figure 11: Distribution of fibril angles before (top) and after (bottom) the process of rasterization. The distribution of angles after rasterization serves as the best case scenario for a ptychographic reconstruction.

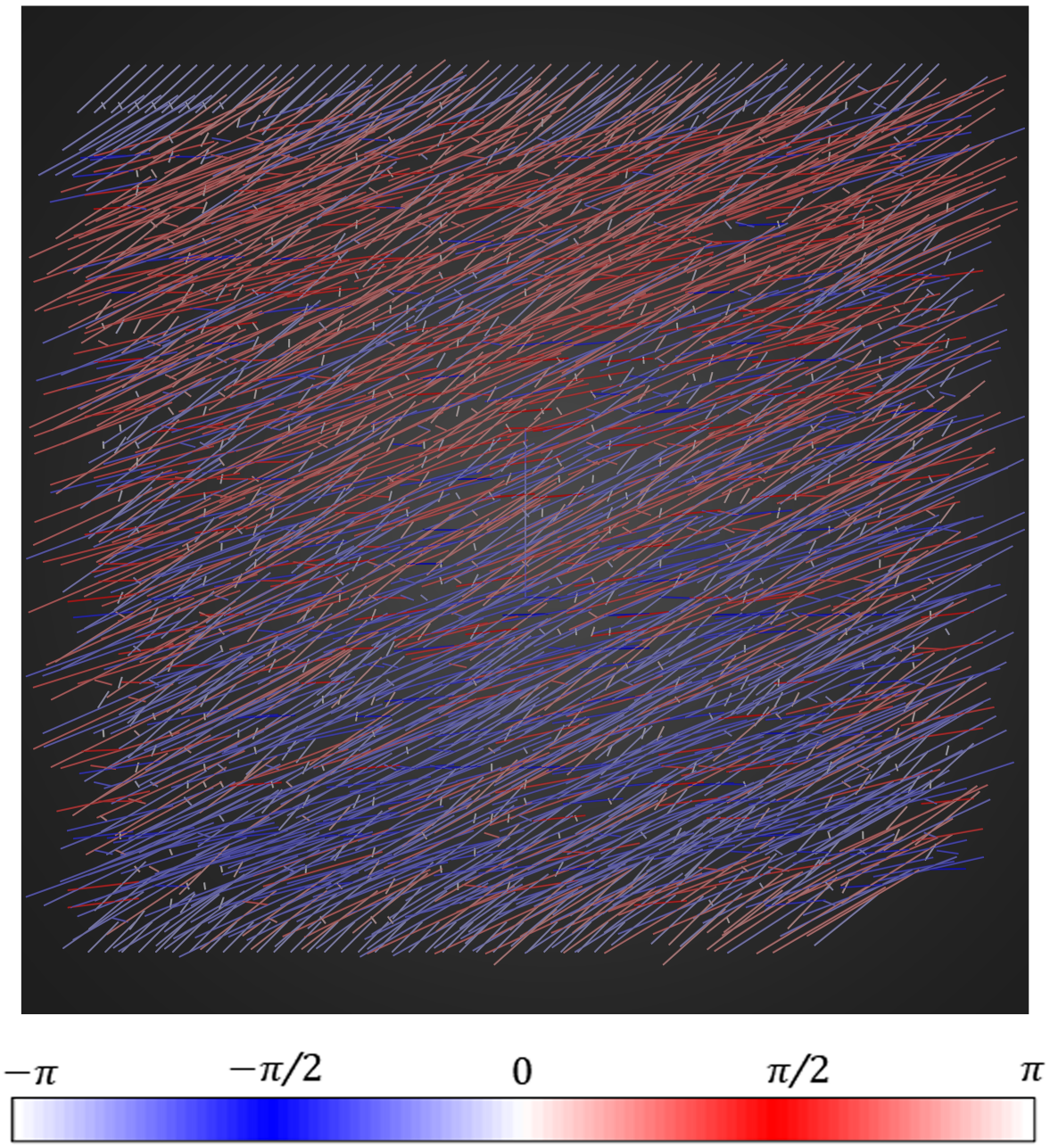

Figure 12: A 3D render of the fibril orientation can be created using data retrieved from the $\chi^{(2)}_{ijk}$ components of the computationally generated sample.

to the number of occurrences of ϕ in the histogram. The color of the effective fibril is chosen according to where its angle appears in the histogram. From the histogram in fig 11.a, we were able to identify the two main peaks at $\phi = -75^o$ and 115^o. Thus, if ϕ is in the range -150^o to -30^o, it is given a color of blue, whereas when ϕ is in the range 30^o to 150^o, it is given a color of red. In this way, we can visualize not only the direction of the fibrils, but also their polarity, since ϕ goes from $-\pi$ to π. This is shown in fig 12, where we see that the rendered sample is visually similar to the heat-map of azimuthal angles but with the addition of length which provides further information about sample alignment. The rendered sample contains a number of very small white fibrils which correspond to fibrils aligned away from the peak regions but with a very low occurrence rates. These short white fibrils indicate an area with no general alignment as they are made of real fibrils with varying degrees of misalignment. By examining the length of rendered effective fibrils we can interpret information about the total alignment of the sample while the color of a fibril provides information about fibril polarity.

From the resulting figures in this subsection, we showed how we generate a sample of collagen fibrils with regions of varying alignment and retrieve information about the alignment of the sample. This demonstration however only illustrates the competency of the generation and angle retrieval modules of our approach. Next we will demonstrate that we can use measurement data gathered from this sample to reconstruct it.

4.2 Numerical Diffraction Pattern Measurements

We consider two numerical apertures, which are feasible in SHG experiments. These are NA= 0.6 and NA= 0.8. We consider 850 probe positions with a spot size of $10\mu m$, 3 probe polarizations $(0^o, 45^o.90^o)$ and three output polarization angles $(0^o, 45^o.90^o)$, so that for each probe position, we have 9 measurements.

In the current state of this model the total amount of required probe positions is on the order of 700 to 900 total probe positions for spot sizes around $10\mu m$ with 9 separate polarization measurements, resulting in 6,300 to 8,100 total measurements being needed for decent reconstruction, this compares favorably to the 2,621,440 required by PSHG under the assumption that 10 polarization measurements are needed for each input beam position, which for confocal geometry has a size that is generally has a size that is typically on order of magnitude smaller than the input beam we are considering. It is possible that with improvement to position distribution that fewer measurements will be required in future versions of the ptychography model.

Before the reconstruction can be performed, a set of measurement data $I^{(m)}(q_x, q_y, \gamma, \nu)$ needs to be created using our numerical sample, which we have done according to the procedure detailed in chapter 3.3. The number of measurements required varies with the parameters of the input beam, specifically the beam waist. For this work our input beam is taken to be a Gaussian beam with a wavelength of 800nm and a waist of $10\mu m$, though larger waist sizes are possible and would likely result in further decreases in the required number of measurements. We take our virtual CCD camera to have a resolution of 512×512 square pixels, and for convenience, we discretize our sample in xy space with the same resolution. Each grid cell in the sample space has an area of $0.01\mu m^2$, so that our total sample area is $51.2 \times 51.2\mu m^2$.

4.3 tPIE Reconstruction

Now that we have our numerical measurements, the tensorial ptychographic reconstruction is performed via the tPIE algorithm outlined in chapter 2.1. We begin with a guess for the four independent object components, $\chi^{(2)}_{xxx}$, $\chi^{(2)}_{xxy} = \chi^{(2)}_{yxx} = \chi^{(2)}_{xyx}$, $\chi^{(2)}_{xyy} = \chi^{(2)}_{yxy} = \chi^{(2)}_{yyx}$, and $\chi^{(2)}_{yyy}$, which we take to each be an array of uniformly distributed random numbers between 0 and 1. As described earlier, for each probe position and polarization state, we calculate the exit-field $\vec{\psi}^{(m)}(x, y, \gamma)$, and its associated far-field $\vec{\Psi}^{(m)}(q_x, q_y, \gamma)$. The output polarizer is then applied to obtain our guessed scalar far-field $\xi^{(m)}(q_x, q_y, \gamma, \nu)$. There will be nine such guessed scalar fields for each probe position. We then create a hybrid scalar far-field which takes its phase from our guessed scalar far-field and its magnitude from the actual measured far-field. This hybrid field is then applied to update the guessed $\chi^{(2)}$ object components.

This update is repeated for all probe positions, then this is repeated for M iterations, where we find M=200 is sufficient to reach convergence. In the end, we obtain a reconstruction of the complex components of the $\overleftrightarrow{\chi}^{(2)}$ tensor can be saved and evaluated.

In order to evaluate the quality of the reconstructed components of the $\overleftrightarrow{\chi}^{(2)}$ tensor we will compare them with the original rasterized sample that was used to create the numerical measurements. Figs [13, 15] show the magnitude and phase, respectively, of the four reconstructed $\overleftrightarrow{\chi}^{(2)}$ components using a measurement set with a numerical aperture of 0.6 and figs [14,16] show these reconstructions for a measurement set with a NA of 0.8. The magnitude plots are scaled according to the maximum and minimum $\overleftrightarrow{\chi}^{(2)}$ values of the numerical sample so that all cases are visually comparable.

Before evaluating the results on a case-by-case basis we first discuss the general fea-

tures present in all reconstructed images. The first common feature is the vignetting (non-reconstructed data along corners) that is present in all reconstructed images. This is not a reconstruction problem but a measurement problem, measurement positions are generated only within a certain range which was not far enough from the center of the image to consistently reconstruct information in the corners. This can be remedied by extending the total distance from the center that measurement positions are chosen from.

First we discuss the reconstruction of the magnitude of the $\overleftrightarrow{\chi}^{(2)}$ tensor components (bottom of Figs [13, 14]) and compare them to the magnitude of the original numerical sample (top of Figs [13, 14], reproduced from fig 9 for convenience). We find that the geometry of the numerical sample is captured well for both the NA of 0.6 and 0.8 cases. There is a distinct blurring in the reconstruction as a result of diffraction, where the degree of the blurring is dependent on the numerical aperture of the measurement, with more blurring present with a lower numerical aperture as one would expect.

The phase of the $\overleftrightarrow{\chi}^{(2)}$ tensor components (bottom of figs [15, 16] for NA = 0.6, 0.8 respectively.) is similarly able to accurately reconstruct the two distinct alignment regions in addition to the region of mixed alignment. The phase of the original numerical sample $\overleftrightarrow{\chi}^{(2)}$ components are reproduced in the top four plots of 15, and 16 for convenience. Due to a global phase factor the coloring of the phase does not exactly line up with that of the sample but the angles between each alignment region are separated by π as in the sample; the four reconstructed components also show the same relative phase as the four numerical sample components. There are imperfections in the reconstruction of phase angles as a result of diffraction creating a smearing effect similar to what was discussed for the magnitude and is also decreased as NA increases. The original sample is real valued and so has a phase that is either 0 or π while the reconstruction is complex and can take a range of phase values. In both cases the reconstruction algorithm is able to reproduce all three distinct alignment regions, and many of the finer details of the original, even if not perfectly.

4.4 Angle Retrieval

Now that we have demonstrated that reconstructions found using tPIE are reasonably similar to the original sample, we use this reconstructed data to gain further information about the sample organization. To this end the last part of our approach that needs to be evaluated is the ability to retrieve information about the in-plane angle ϕ from a reconstructed data-set, as described in chapter 2.2. The primary means of evaluating

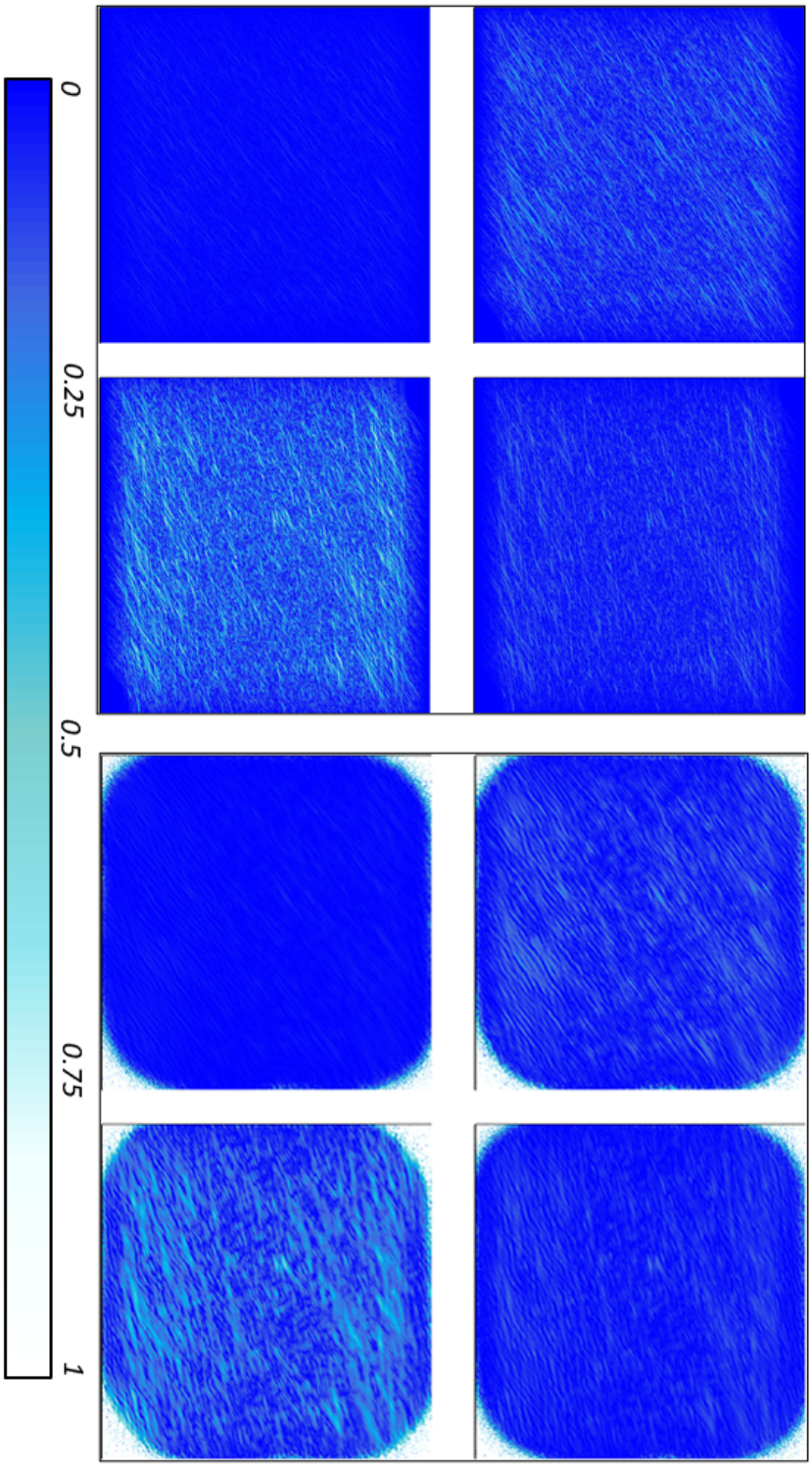

Figure 13: Magnitude of reconstructed (bottom) $\chi^{(2)}_{ijk}$ components using 850 measurement positions with a numerical aperture of 0.6 compared to the original sample magnitude (top)

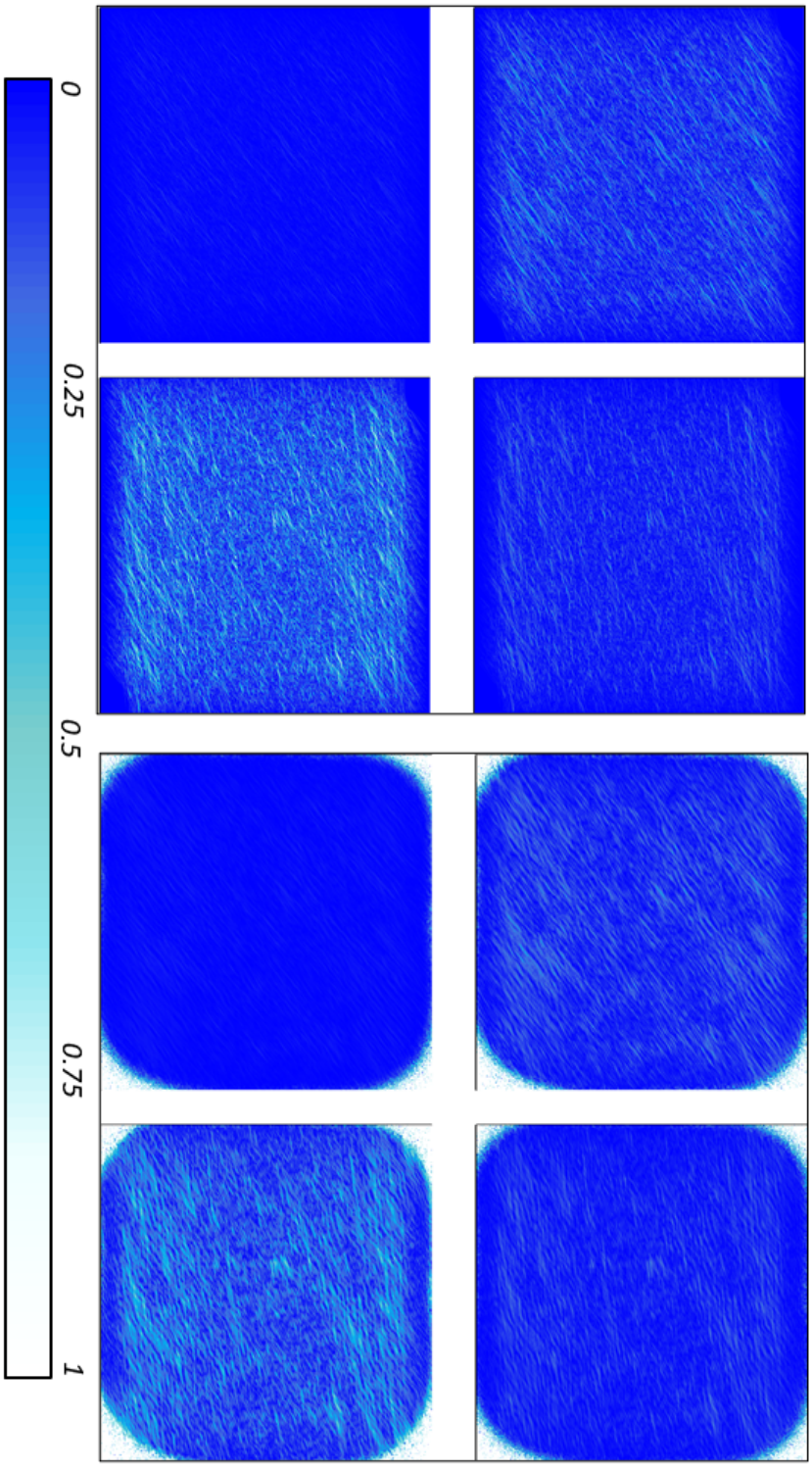

Figure 14: Magnitude of reconstructed (bottom) $\chi^{(2)}_{ijk}$ components using 850 measurement positions with a numerical aperture of 0.8 compared to the original sample magnitude (top)

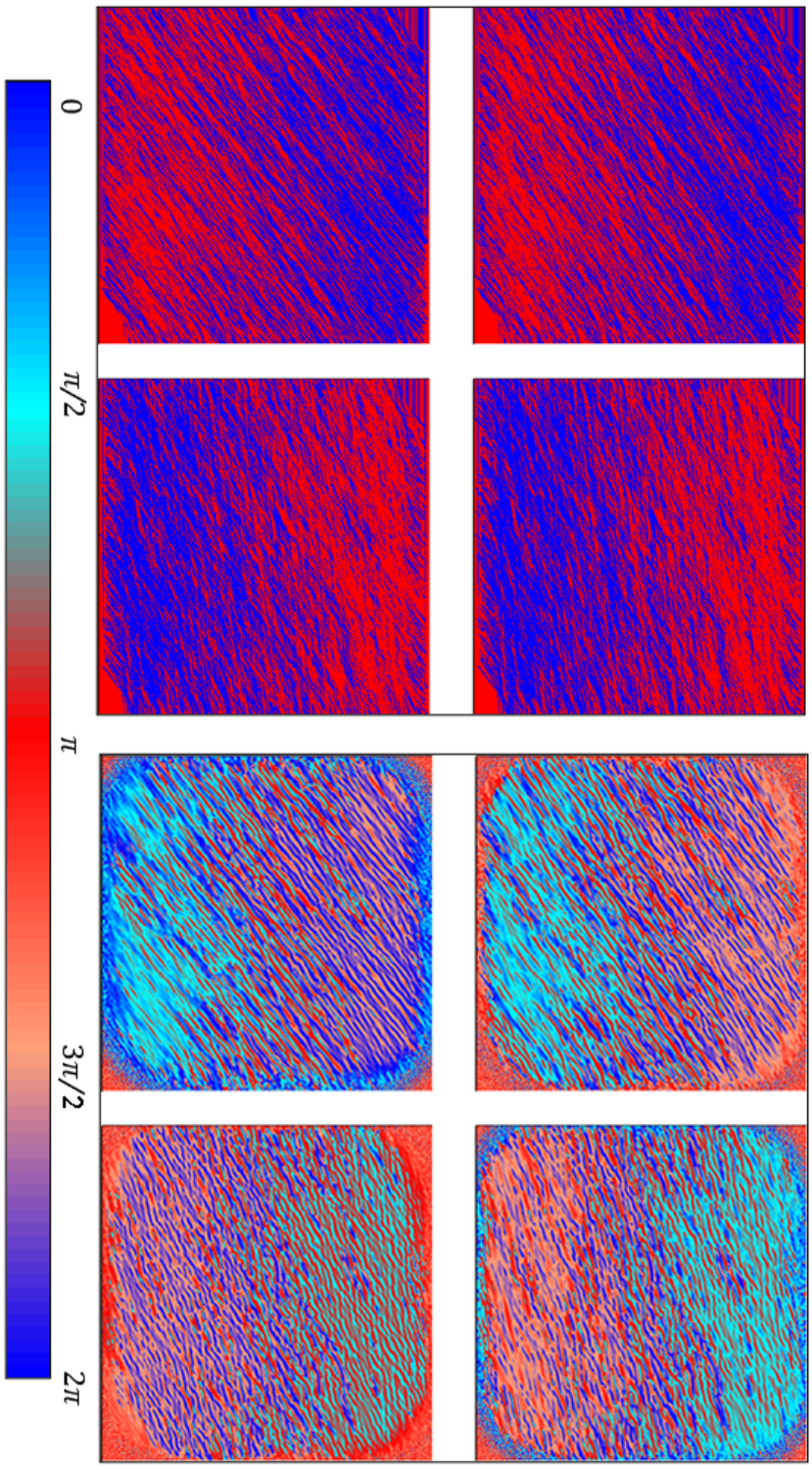

Figure 15: Phase of reconstructed (bottom) $\chi^{(2)}_{ijk}$ components using 850 measurement positions with a numerical aperture of 0.6 compared to the original sample phase (top)

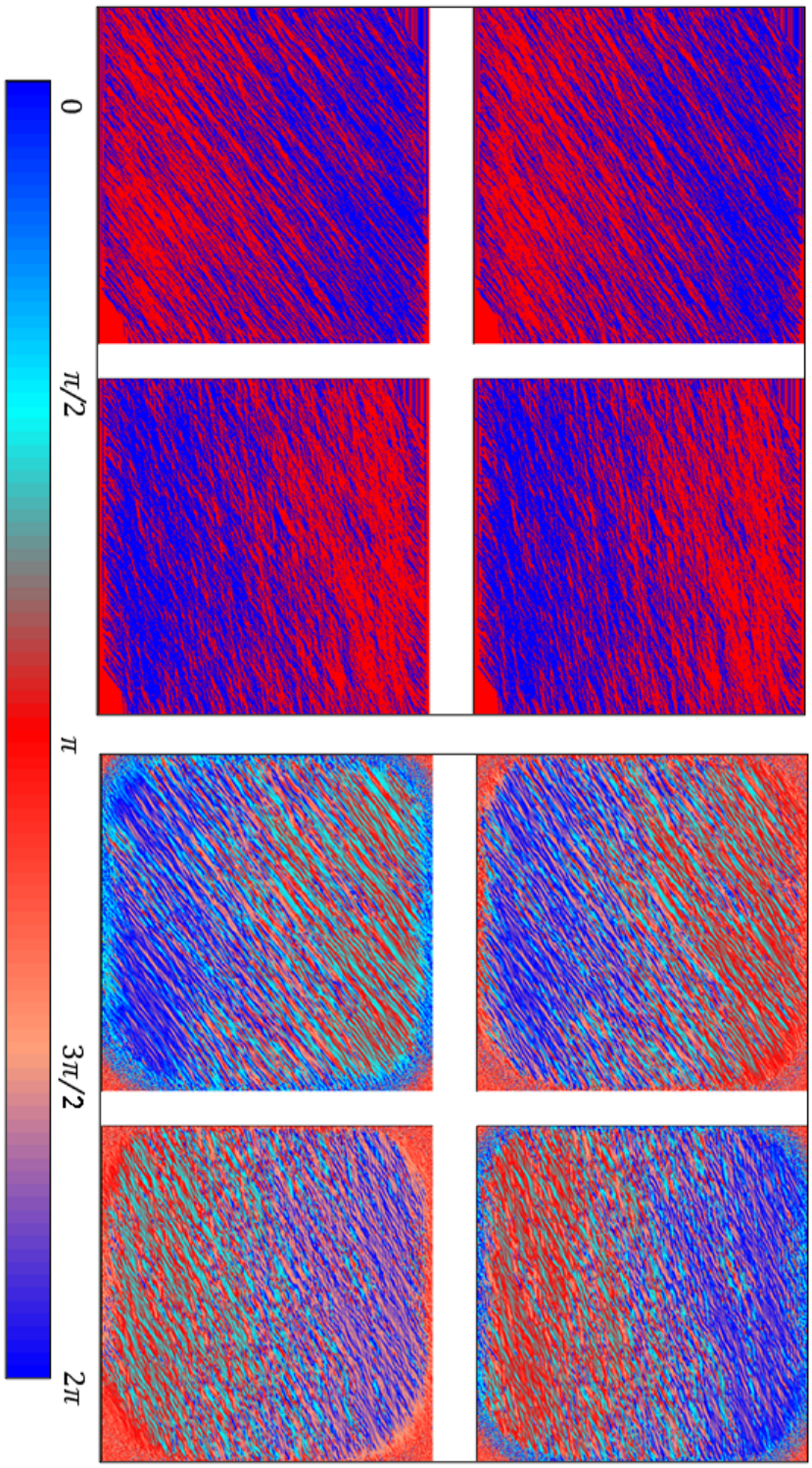

Figure 16: Phase of reconstructed (bottom) $\chi^{(2)}_{ijk}$ components using 850 measurement positions with a numerical aperture of 0.8 compared to the original sample phase (top)

this aspect is to produce a map of ϕ and compare it to the map presented in section 4.1 for the original numerical sample. Figures [17, 18] show both the reconstructed ϕ heatmaps (bottom) and the original ϕ heat maps (top, reproduced here for convenience) for the NA=0.6 and 0.8 cases, respectively. Recall that our $\overleftrightarrow{\chi}^{(2)}$ reconstructed phases in figures [15, 16] are able to reasonably reconstruct the three distinct alignment regions of the sample with blurring induced by diffraction and color smearing, However, this color smearing is not observed in the reconstructed ϕ heatmaps of figures [17, 18].

The heatmap of azimuthal angles provides a significant amount of information otherwise assumed to be lost in imaging, specifically the alignment and polarity of an effective fibril. From the phase alone we can discern the polarity of a fibril which is very useful determining collagen alignment but the retrieval of the azimuthal and polar angles additionally provide organizational information. Using angle retrieval we can determine not only that there are three regions of collagen alignment in a sample using only intensity measurement data but also how that sample is structured by analyzing the angular information.

Next we compare in figures [19,20] for NA-0.6 and 0.8, respectively, the histograms for the ϕ angle distributions over the sample as extracted from the ptychographic reconstructions (bottom plots) to that produced by the rasterized numerical sample (top plots, reproduced here from fig 11 for convenience). In both cases, the histograms are accurately reproduced as a bi-modal normal distribution.

Finally, we use the reconstructed data to produce a 3D render using the same procedure as we used to produce a render from the original numerical sample in fig 12 described in section 4.1. This render was produced by the reconstructed data set using the measurement set with a numerical aperture of 0.8. Comparing to the render produced for the numerical sample, the reconstructed data set is able to produce a reasonable render depicting the regions of fibril alignment and organization in the sample.

In this work we have shown that we are able to generate a sample of collagen fibrils with regions of varying alignment reasonably and that this model can be analyzed to recover information about both alignment and organization. The primary result of this work is that using our newly developed tensorial Ptychographical iterative engine (tPIE) we are able to account for the tensorial nature of the nonlinear optical susceptibility, and not only reconstruct the tensor components of $\overleftrightarrow{\chi}^{(2)}$ including the otherwise lost phase information, but are able to use this reconstructed information to retrieve new information about the organization of sample based only on a set of wide-field polarization

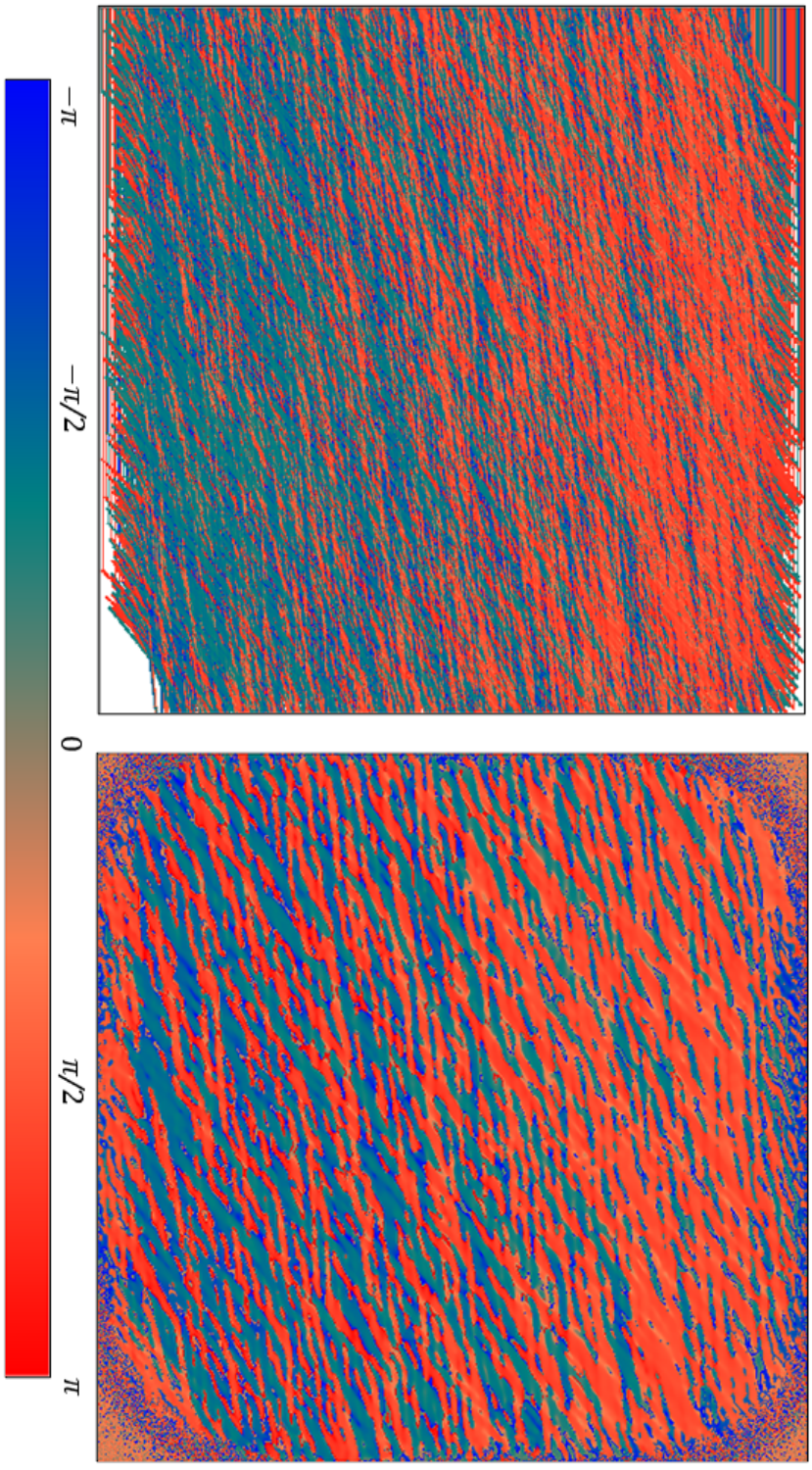

Figure 17: Azimuthal angle map retrieved from reconstructed (bottom) $\chi^{(2)}_{ijk}$ components using 850 measurement positions with a numerical aperture of 0.6 compared to the azimuthal angle map retrieved from the original sample magnitude (top)

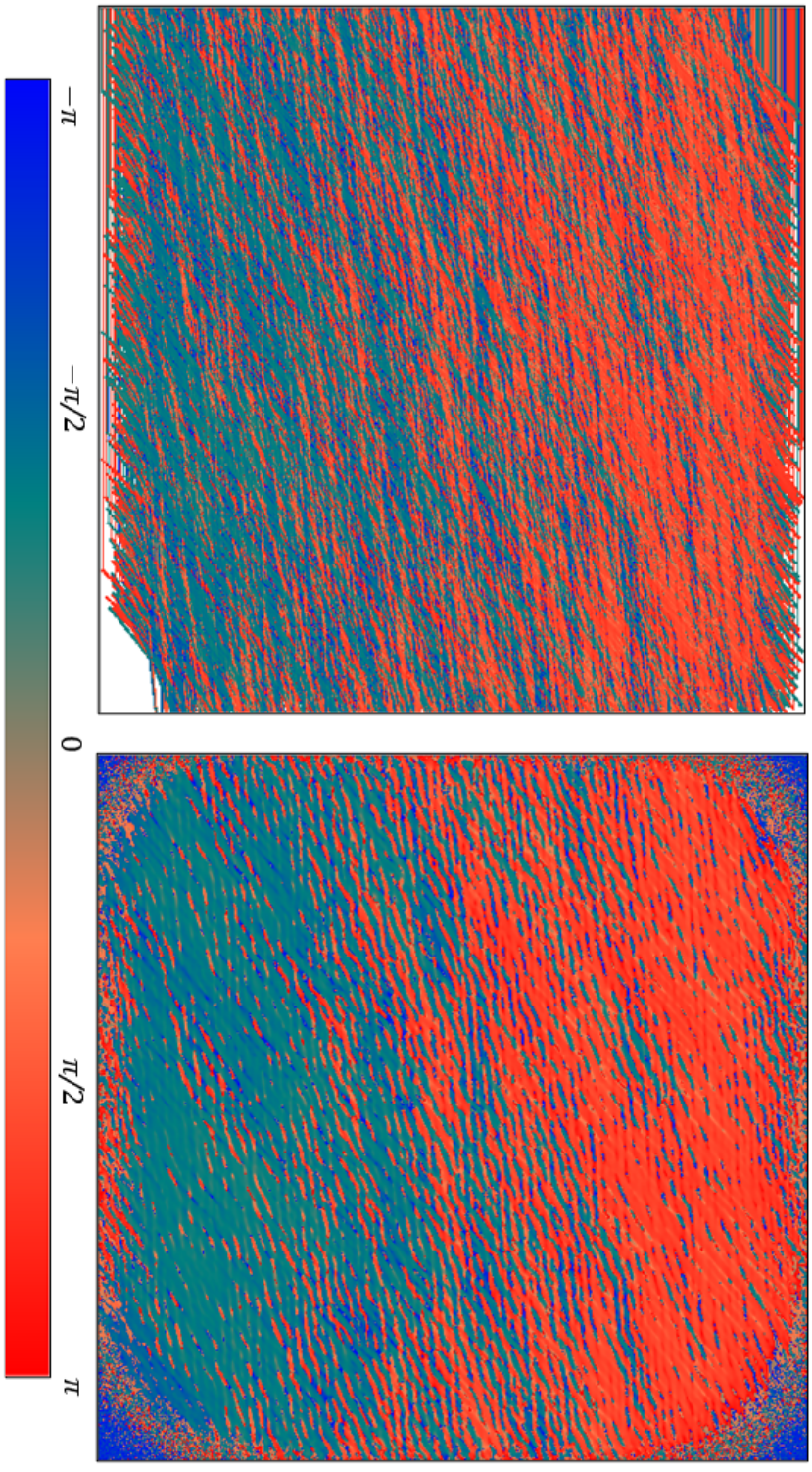

Figure 18: Azimuthal angle map retrieved from reconstructed (bottom) $\chi^{(2)}_{ijk}$ components using 850 measurement positions with a numerical aperture of 0.8 compared to the azimuthal angle map retrieved from the original sample magnitude (top)

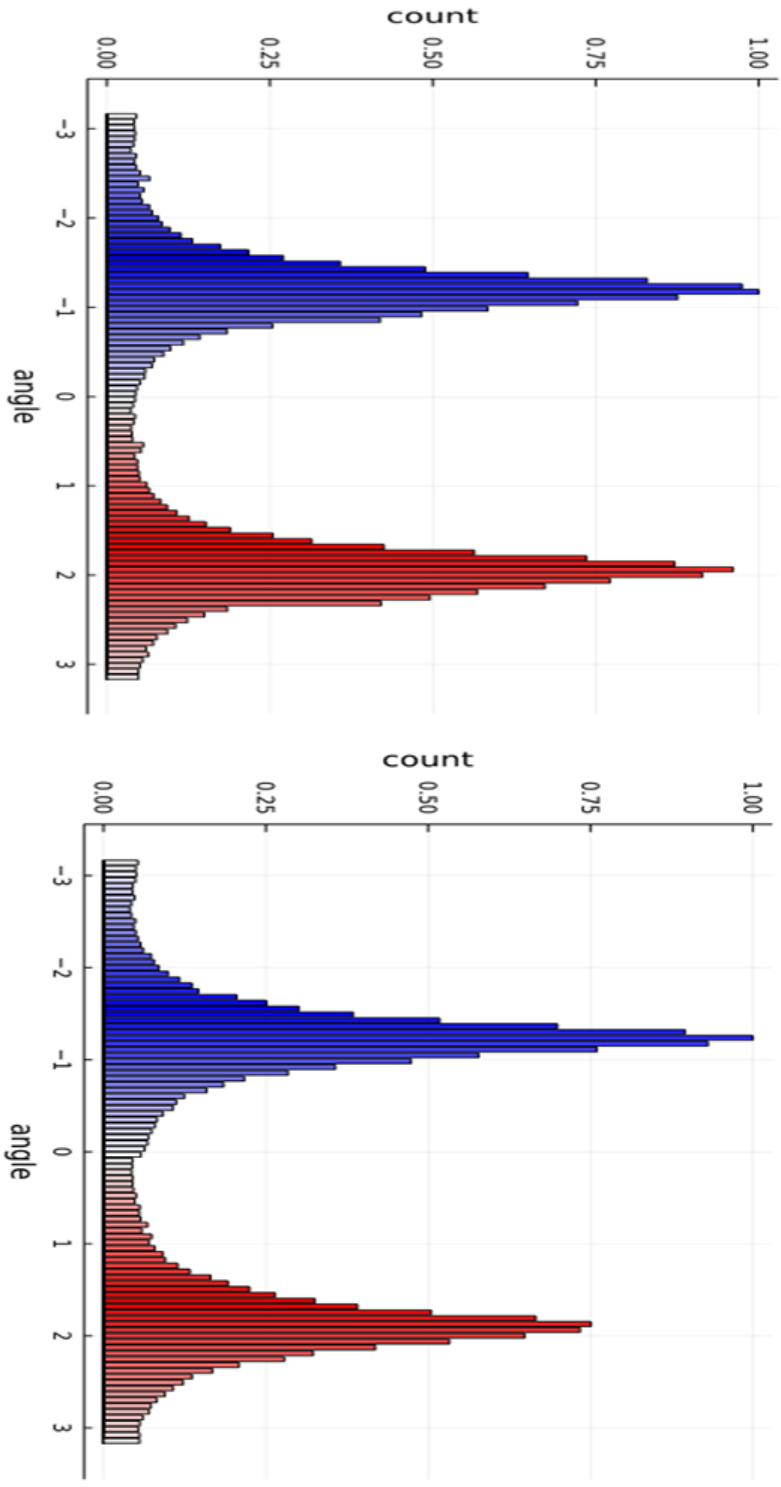

Figure 19: Distribution of azimuthal angles retrieved from reconstructed (bottom) $\chi^{(2)}_{ijk}$ components using 850 measurement positions with a numerical aperture of 0.6 compared to the azimuthal distribution retrieved from the original sample (top)

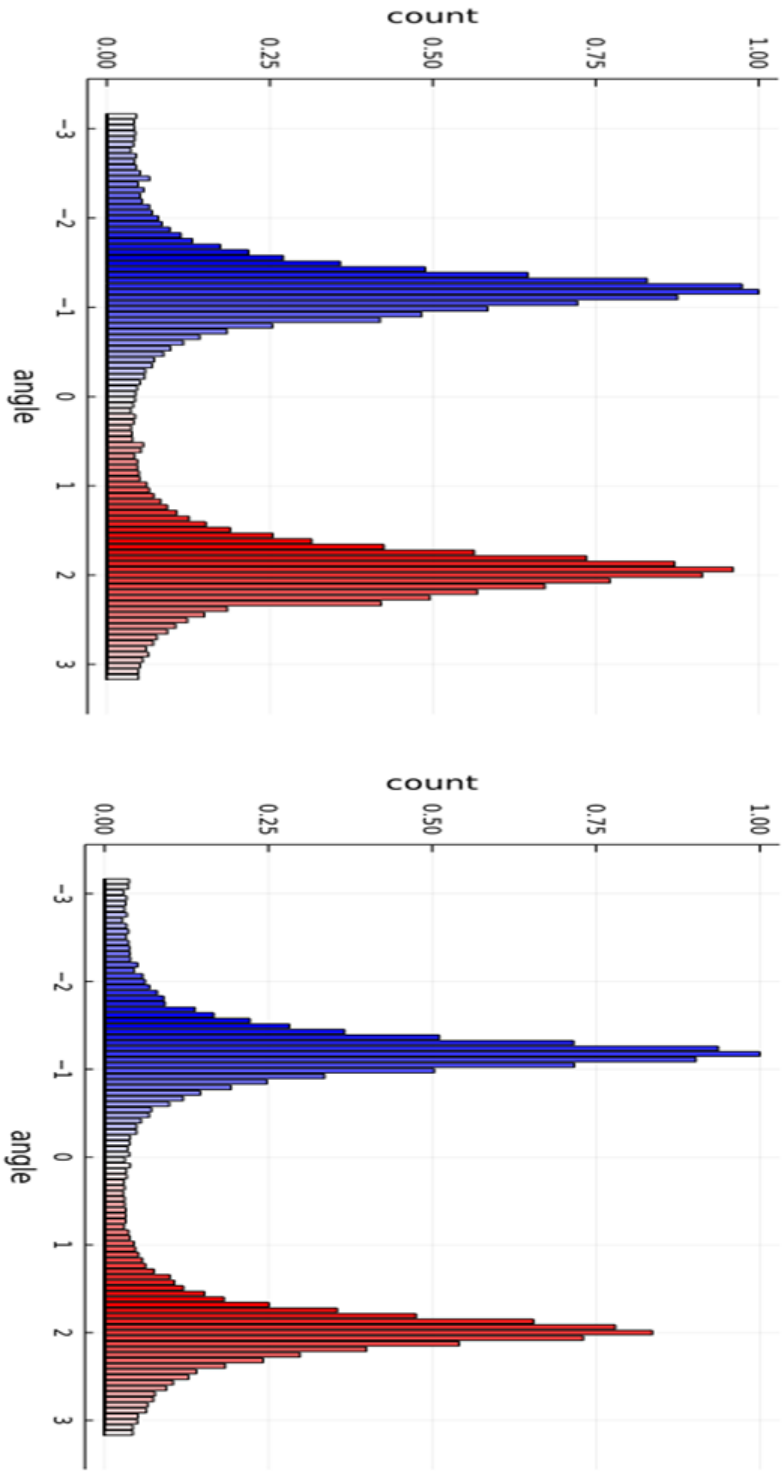

Figure 20: Distribution of azimuthal angles retrieved from reconstructed (bottom) $\chi^{(2)}_{ijk}$ components using 850 measurement positions with a numerical aperture of 0.8 compared to the azimuthal distribution retrieved from the original sample (top)

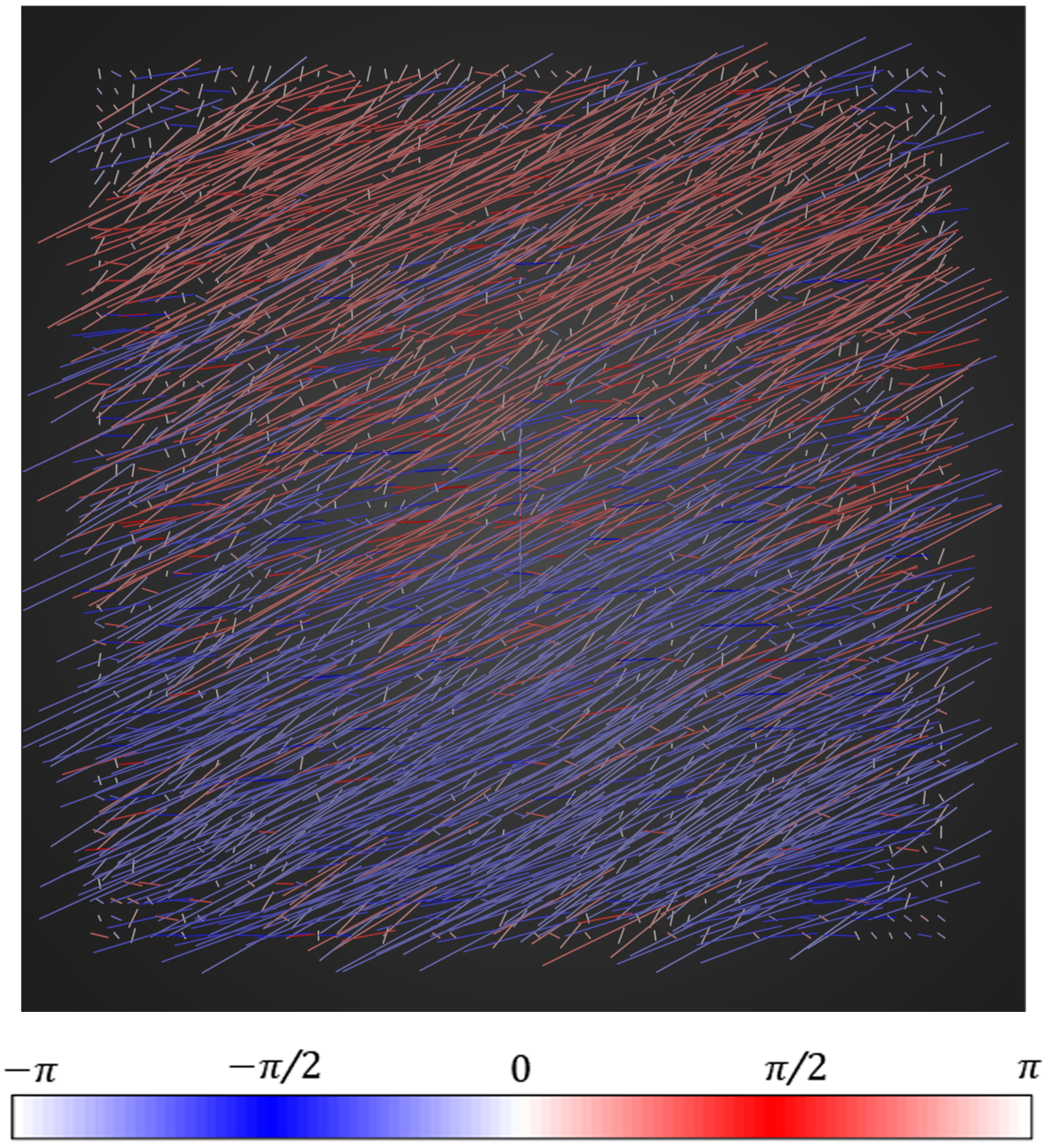

Figure 21: 3D render of sample generated using data retrieved from reconstructed $\chi^{(2)}_{ijk}$ components using 850 measurement positions with a numerical aperture of 0.8

images. We can accomplish this without requiring a stable reference beam or complex optical configurations as required by both interferometry and PSHG. Moreover this can be performed with fewer measurements as we are no longer restricted to a confocal geometry.

5

Conclusion

Traditional fluorescent microscopy methods are an indispensable tool in the life sciences due to its high resolution and sensitivity in many materials. These traditional methods are further boosted by the introduction of fluorescent staining to extend the compatible materials even further. The high resolution of fluorescent microscopy has also been enhanced through novel methods including; Stimulated Emission Depletion (STED) microscopy, Structured Illumination Microscopy (SIM), Stochastic Optical Reconstruction Microscopy (STORM) and Photo-Activated Localization Microscopy. However this powerful tool is not perfect, there are a wide class of materials that cannot be imaged with fluorescence and cannot be dyed without influencing the dynamics of the process of interest. Furthermore fluorescent microscopy is often limited to the confocal geometry which restricts the spot size of the illumination and in turn requires many additional measurements be taken for a single image.

In this thesis to address this need with discuss Second Harmonic Generation (SHG) microscopy, a coherent nonlinear optical imaging process. I describe the extreme sensitivity of SHG signals to collagen alignment and how it is prudent to exploit this sensitivity to obtain an angular description of a collagen sample. I discussed some existing methods in SHG microscopy, interferometric SHG (iSHG) which allows the recovery of phase,

and polarization SHG (pSHG) which recovers alignment information. There are however drawbacks in both iSHG; the need for a stable reference beam, a required confocal geometry, and the many measurements needed to recover phase; and pSHG; a complex optical system; the confocal geometry, and a very high number of measurements. To address the shortcomings of these methods we introduced ptychography for coherent nonlinear optical microscopy, which allows for the recovery of phase without the need for a stable reference beam and sample orientation with fewer measurements than pSHG. Ptychography is designed for lensless microscopy systems and is not restricted to the confocal geometry.

The generation of a numerical collagen sample was described in detail and demonstrated by creating a sample with 30,000 collagen fibrils with three regions of alignment, two aligned regions and a region of mixed alignment. Using this sample I demonstrated that using the angle retrieval model detailed in section 2.2 it is possible to retrieve information about sample organization using only the complex components of the nonlinear optical susceptibility. This numerical sample is then used to generate a set of diffractive measurements using the numerical diffraction model detailed in section 3.3. The numerical measurement set was applied to the ptychography model detailed in sections 3.1 and 3.2, finally the reconstructed components of the nonlinear optical susceptibility were used to demonstrate the angle retrieval model on reconstructed information.

The results of these demonstrations illustrated that I am able to numerically generate a sample of collagen fibrils with three distinct regions of alignment which I can then retrieve the alignment information accurately from using only the corresponding components of the nonlinear optical susceptibility, this result was then used as a validation of ptychographically reconstructed nonlinear optical susceptibility components. when comparing the reconstructed components with the sample components a very high accuracy was observed with imperfections due to diffraction. From these result I conclude that the tensorial Ptychographical iterative engine (tPIE) developed in this work offers a valid methodology for phase recovery of the multiple components of the nonlinear optical susceptibility tensor. I further demonstrated that using only the complex components of the nonlinear optical susceptibility tensor the angular retrieval model is able to accurately produce organization information of a sample with fewer required measurement than existing techniques. In the future I plan to extend this model for alternative optical imaging techniques, apply this technique to experimentally measured data, and design a system to easily integrate this system into an existing microscopy environment.

References

[1] Coons, A. *The Demonstration of Pneumococcal Antigen in Tissues by the Use of Fluorescent Antibody.* The Journal of Immunology, **45**(3):159–170 (1942). ISSN 0022-1767, 1550-6606. https://www.jimmunol.org/content/45/3/159. (Cited on page 1.)

[2] Wang, W. *et al. Single Cell Behavior in Metastatic Primary Mammary Tumors Correlated with Gene Expression Patterns Revealed by Molecular Profiling.* Cancer Research, **62**(21):6278–6288 (2002). ISSN 0008-5472, 1538-7445. https://cancerres.aacrjournals.org/content/62/21/6278. (Cited on pages 1, 3, and 7.)

[3] Masters, B. *et al. Multiphoton excitation fluorescence microscopy and spectroscopy of in vivo human skin.* Biophysical Journal, **72**(6):2405–2412 (1997). ISSN 00063495. http://dx.doi.org/10.1016/S0006-3495(97)78886-6. (Cited on page 1.)

[4] Barentine, A.E. *et al. Simultaneously Measuring Image Features and Resolution in Live-Cell STED Images.* Biophysical Journal, **115**(6):951–956 (2018). ISSN 00063495. http://dx.doi.org/10.1016/j.bpj.2018.07.028. (Cited on page 1.)

[5] Piston, D. *Imaging living cells and tissues by two-photon excitation microscopy.* Trends in Cell Biology, **9**(2):66–69 (1999). ISSN 09628924. http://dx.doi.org/10.1016/S0962-8924(98)01432-9. (Cited on page 1.)

[6] Carlsson, K. *et al. Three-dimensional microscopy using a confocal laser scanning microscope.* Optics Letters, **10**(2):53 (1985). ISSN 0146-9592, 1539-4794. http://dx.doi.org/10.1364/OL.10.000053. (Cited on page 1.)

[7] Masters, B.R. *Three-dimensional confocal microscopy of the human optic nerve in vivo.* Optics Express, **3**(10):356 (1998). ISSN 1094-4087. http://dx.doi.org/10.1364/OE.3.000356. (Cited on page 1.)

[8] Vaknin, A. and Berg, H.C. *Single-cell FRET imaging of phosphatase activity in the Escherichia coli chemotaxis system.* Proceedings of the National Academy of Sciences, **101**(49):17072–17077 (2004). (Cited on page 1.)

[9] Feng, H. *et al. Super-Resolution Fluorescence Microscopy for Single Cell Imaging*. In J. Gu and X. Wang, editors, *Single Cell Biomedicine*, volume 1068, pages 59–71. Springer Singapore, Singapore (2018). ISBN 9789811305016 9789811305023. http://dx.doi.org/10.1007/978-981-13-0502-3_6. (Cited on page 1.)

[10] Sun, Y. and Periasamy, A. *Fluorescence Microscopy Imaging in Biomedical Sciences*. In R. Liang, editor, *Biomedical Optical Imaging Technologies*, pages 79–110. Springer Berlin Heidelberg, Berlin, Heidelberg (2013). ISBN 9783642283901 9783642283918. http://dx.doi.org/10.1007/978-3-642-28391-8_3. (Cited on page 1.)

[11] Hell, S.W. and Wichmann, J. *Breaking the diffraction resolution limit by stimulated emission: stimulated-emission-depletion fluorescence microscopy*. Optics Letters, **19**(11):780–782 (1994). ISSN 1539-4794. http://dx.doi.org/10.1364/OL.19.000780. (Cited on page 2.)

[12] Vicidomini, G. *et al. STED super-resolved microscopy*. Nature Methods, **15**(3):173–182 (2018). ISSN 1548-7105. http://dx.doi.org/10.1038/nmeth.4593. (Cited on page 2.)

[13] Nägerl, U.V. *et al. Live-cell imaging of dendritic spines by STED microscopy*. Proceedings of the National Academy of Sciences, **105**(48):18982–18987 (2008). (Cited on page 2.)

[14] D'Este, E. *et al. STED Nanoscopy Reveals the Ubiquity of Subcortical Cytoskeleton Periodicity in Living Neurons*. Cell Reports, **10**(8):1246–1251 (2015). ISSN 22111247. http://dx.doi.org/10.1016/j.celrep.2015.02.007. (Cited on page 2.)

[15] Saxena, M. *et al. Structured illumination microscopy*. Advances in Optics and Photonics, **7**(2):241 (2015). ISSN 1943-8206. http://dx.doi.org/10.1364/AOP.7.000241. (Cited on page 2.)

[16] Hirvonen, L.M. *et al. Structured illumination microscopy of a living cell*. European Biophysics Journal, **38**(6):807–812 (2009). ISSN 0175-7571, 1432-1017. http://dx.doi.org/10.1007/s00249-009-0501-6. (Cited on page 2.)

[17] Rust, M.J. *et al. Sub-diffraction-limit imaging by stochastic optical reconstruction microscopy (STORM)*. Nature Methods, **3**(10):793–796 (2006). ISSN 1548-7105. http://dx.doi.org/10.1038/nmeth929. (Cited on page 2.)

[18] Huang, B. *et al. Three-Dimensional Super-Resolution Imaging by Stochastic Optical Reconstruction Microscopy.* Science, **319**(5864):810–813 (2008). ISSN 0036-8075, 1095-9203. http://dx.doi.org/10.1126/science.1153529. (Cited on page 2.)

[19] Hess, S.T. *et al. Ultra-High Resolution Imaging by Fluorescence Photoactivation Localization Microscopy.* Biophysical Journal, **91**(11):4258–4272 (2006). ISSN 00063495. http://dx.doi.org/10.1529/biophysj.106.091116. (Cited on page 2.)

[20] Gould, T.J. *et al. Imaging biological structures with fluorescence photoactivation localization microscopy.* Nature Protocols, **4**(3):291–308 (2009). ISSN 1754-2189, 1750-2799. http://dx.doi.org/10.1038/nprot.2008.246. (Cited on page 2.)

[21] Boyd, R.W. *Nonlinear optics.* Academic Press, Amsterdam ; Boston, 3rd ed edition (2008). ISBN 9780123694706. https://www-sciencedirect-com.proxy.bib.uottawa.ca/book/9780121216825/nonlinear-optics. (Cited on pages 2 and 8.)

[22] Pavone, F.S. and Campagnola, P.J. *Second Harmonic Generation Imaging.* CRC Press, 1 edition (2013). ISBN 9780367379902. https://www-taylorfrancis-com.proxy.bib.uottawa.ca/books/mono/10.1201/b15039/second-harmonic-generation-imaging-francesco-pavone-paul-campagnola. (Cited on pages 2 and 3.)

[23] Dombeck, D.A. *et al. Optical Recording of Fast Neuronal Membrane Potential Transients in Acute Mammalian Brain Slices by Second-Harmonic Generation Microscopy.* Journal of Neurophysiology, **94**(5):3628–3636 (2005). ISSN 0022-3077. http://dx.doi.org/10.1152/jn.00416.2005. (Cited on page 2.)

[24] Moreaux, L. *et al. Membrane imaging by second-harmonic generation microscopy.* Journal of the Optical Society of America B, **17**(10):1685 (2000). ISSN 0740-3224, 1520-8540. http://dx.doi.org/10.1364/JOSAB.17.001685. (Cited on page 2.)

[25] Shoulders, M.D. and Raines, R.T. *Collagen Structure and Stability.* Annual Review of Biochemistry, **78**(1):929–958 (2009). ISSN 0066-4154. http://dx.doi.org/10.1146/annurev.biochem.77.032207.120833. (Cited on page 3.)

[26] Zipfel, W.R. *et al. Nonlinear magic: multiphoton microscopy in the biosciences.* Nature Biotechnology, **21**(11):1369–1377 (2003). ISSN 1546-1696. http://dx.doi.org/10.1038/nbt899. (Cited on pages 3 and 7.)

[27] Troeberg, L. and Nagase, H. *Proteases involved in cartilage matrix degradation in osteoarthritis*. Biochimica et Biophysica Acta (BBA) - Proteins and Proteomics, **1824**(1):133–145 (2012). ISSN 15709639. http://dx.doi.org/10.1016/j.bbapap.2011.06.020. (Cited on pages 3 and 7.)

[28] Yazdanfar, S. *et al. Interferometric second harmonic generation microscopy*. Optics Express, **12**(12):2739 (2004). ISSN 1094-4087. http://dx.doi.org/10.1364/OPEX.12.002739. (Cited on page 4.)

[29] Bancelin, S. *et al. Fast interferometric second harmonic generation microscopy*. Biomedical Optics Express, **7**(2):399 (2016). ISSN 2156-7085, 2156-7085. http://dx.doi.org/10.1364/BOE.7.000399. (Cited on page 4.)

[30] Couture, C.A. *et al. The Impact of Collagen Fibril Polarity on Second Harmonic Generation Microscopy*. Biophysical Journal, **109**(12):2501–2510 (2015). ISSN 00063495. http://dx.doi.org/10.1016/j.bpj.2015.10.040. (Cited on pages 4 and 7.)

[31] Amat-Roldan, I. *et al. Fast image analysis in polarization SHG microscopy*. Optics Express, **18**(16):17209 (2010). ISSN 1094-4087. http://dx.doi.org/10.1364/OE.18.017209. (Cited on page 4.)

[32] Houle, M.A. *et al. Analysis of forward and backward Second Harmonic Generation images to probe the nanoscale structure of collagen within bone and cartilage*. Journal of Biophotonics, **8**(11-12):993–1001 (2015). ISSN 1864-0648. http://dx.doi.org/https://doi.org/10.1002/jbio.201500150. (Cited on pages 4, 7, and 19.)

[33] Seo, M. *et al. Ultrafast optical wide field microscopy*. Optics Express, **21**(7):8763 (2013). ISSN 1094-4087. http://dx.doi.org/10.1364/OE.21.008763. (Cited on page 4.)

[34] Cox, G. and Sheppard, C.J.R. *Practical limits of resolution in confocal and non-linear microscopy*. Microscopy Research and Technique, **63**(1):18–22 (2004). ISSN 1097-0029. http://dx.doi.org/10.1002/jemt.10423. (Cited on page 4.)

[35] Zhao, H. *et al. Live imaging of contracting muscles with wide-field second harmonic generation microscopy using a high power laser*. Biomedical Optics Express, **10**(10):5130 (2019). ISSN 2156-7085, 2156-7085. http://dx.doi.org/10.1364/BOE.10.005130. (Cited on page 4.)

[36] Dementjev, A. *et al.* *Optimization of wide-field second-harmonic generation microscopy for fast imaging of large sample areas in biological tissues*. Lithuanian Journal of Physics, **60**(3) (2020). ISSN 2424-3647. http://dx.doi.org/10.3952/physics.v60i3.4301. (Cited on page 4.)

[37] Rodenburg, J.M. and Faulkner, H.M.L. *A phase retrieval algorithm for shifting illumination*. Applied Physics Letters, **85**(20):4795–4797 (2004). ISSN 0003-6951. http://dx.doi.org/10.1063/1.1823034. (Cited on pages 4 and 18.)

[38] Odstrcil, M. *et al.* *Nonlinear ptychographic coherent diffractive imaging*. Optics Express, **24**(18):20245–20252 (2016). ISSN 1094-4087. http://dx.doi.org/10.1364/OE.24.020245. (Cited on pages 5 and 19.)

[39] van der Kolk, J.N. and Ramunno, L. *Ptychography for Nonlinear Optical Microscopy: Retrieving Phase without Interferometry*. In *Optics in the Life Sciences Congress*, page NTu3C.1. OSA, San Diego, California (2017). ISBN 9781943580255. http://dx.doi.org/10.1364/NTM.2017.NTu3C.1. (Cited on page 5.)

[40] Ferrand, P. *et al.* *Ptychography in anisotropic media*. Optics Letters, **40**(22):5144–5147 (2015). ISSN 1539-4794. http://dx.doi.org/10.1364/OL.40.005144. (Cited on pages 5, 19, and 26.)

[41] Baroni, A. *et al.* *Joint estimation of object and probes in vectorial ptychography*. Optics Express, **27**(6):8143–8152 (2019). ISSN 1094-4087. http://dx.doi.org/10.1364/OE.27.008143. (Cited on pages 5 and 19.)

[42] Erikson, A. *et al.* *Quantification of the second-order nonlinear susceptibility of collagen I using a laser scanning microscope*. Journal of Biomedical Optics, **12**(4):044002 (2007). ISSN 10833668. http://dx.doi.org/10.1117/1.2772311. (Cited on pages 7, 8, and 15.)

[43] williams. *Interpreting Second-Harmonic Generation Images of Collagen I Fibrils*. Biophysical Journal, **88**(2):1377–1386 (2005). ISSN 0006-3495. http://dx.doi.org/10.1529/biophysj.104.047308. (Cited on page 7.)

[44] Stoller, P. *et al.* *Quantitative second-harmonic generation microscopy in collagen*. Applied Optics, **42**(25):5209 (2003). ISSN 0003-6935, 1539-4522. http://dx.doi.org/10.1364/AO.42.005209. (Cited on page 7.)

[45] lacomb. *Quantitative Second Harmonic Generation Imaging of the Diseased State Osteogenesis Imperfecta: Experiment and Simulation.* Biophysical Journal, **94**(11):4504–4514 (2008). ISSN 0006-3495. http://dx.doi.org/10.1529/biophysj.107.114405. (Cited on page 7.)

[46] Brown, C.P. *et al. Imaging and modeling collagen architecture from the nano to micro scale.* Biomedical Optics Express, **5**(1):233–243 (2014). ISSN 2156-7085. http://dx.doi.org/10.1364/BOE.5.000233. (Cited on page 7.)

[47] Mansfield, J.C. *et al. Collagen reorganization in cartilage under strain probed by polarization sensitive second harmonic generation microscopy.* Journal of The Royal Society Interface, **16**(150):20180611 (2019). ISSN 1742-5689, 1742-5662. http://dx.doi.org/10.1098/rsif.2018.0611. (Cited on page 7.)

[48] Rivard, M. *et al. Imaging the noncentrosymmetric structural organization of tendon with Interferometric Second Harmonic Generation microscopy: Tissue imaging with Interferometric Second Harmonic Generation microscopy.* Journal of Biophotonics, **7**(8):638–646 (2014). ISSN 1864063X. http://dx.doi.org/10.1002/jbio.201300036. (Cited on pages 7, 11, and 19.)

[49] Teulon, C. *et al. Probing the 3D structure of cornea-like collagen liquid crystals with polarization-resolved SHG microscopy.* Optics Express, **24**(14):16084–16098 (2016). ISSN 1094-4087. http://dx.doi.org/10.1364/OE.24.016084. (Cited on page 7.)

[50] Stoller. *Polarization-Modulated Second Harmonic Generation in Collagen.* Biophysical Journal, **82**(6):3330–3342 (2002). ISSN 0006-3495. http://dx.doi.org/10.1016/S0006-3495(02)75673-7. (Cited on page 8.)

[51] Harnagea, C. *et al. Two-Dimensional Nanoscale Structural and Functional Imaging in Individual Collagen Type I Fibrils.* Biophysical Journal, **98**(12):3070–3077 (2010). ISSN 0006-3495. http://dx.doi.org/10.1016/j.bpj.2010.02.047. (Cited on page 11.)

[52] Rodenburg. *Transmission microscopy without lenses for objects of unlimited size.* Ultramicroscopy, **107**(2-3):227–231 (2007). ISSN 0304-3991. http://dx.doi.org/10.1016/j.ultramic.2006.07.007. (Cited on page 18.)

[53] Rodenburg. *Ptychography and Related Diffractive Imaging Methods*. Advances in Imaging and Electron Physics, **150**:87–184 (2008). ISSN 1076-5670. http://dx.doi.org/10.1016/S1076-5670(07)00003-1. (Cited on page 18.)

[54] Maiden. *An improved ptychographical phase retrieval algorithm for diffractive imaging*. Ultramicroscopy, **109**(10):1256–1262 (2009). ISSN 0304-3991. http://dx.doi.org/10.1016/j.ultramic.2009.05.012. (Cited on pages 18 and 19.)

[55] Hoppe, W. *Beugung im inhomogenen Primärstrahlwellenfeld. III. Amplituden- und Phasenbestimmung bei unperiodischen Objekten*. Acta Crystallographica Section A: Crystal Physics, Diffraction, Theoretical and General Crystallography, **25**(4):508–514 (1969). ISSN 0567-7394. http://dx.doi.org/10.1107/S0567739469001069. (Cited on page 18.)

[56] Hegerl, R. and Hoppe, W. *Dynamische Theorie der Kristallstrukturanalyse durch Elektronenbeugung im inhomogenen Primärstrahlwellenfeld*. Berichte der Bunsengesellschaft für physikalische Chemie, **74**(11):1148–1154 (1970). ISSN 0005-9021. http://dx.doi.org/https://doi.org/10.1002/bbpc.19700741112. (Cited on page 18.)

[57] Nellist. *Beyond the conventional information limit: the relevant coherence function*. Ultramicroscopy, **54**(1):61–74 (1994). ISSN 0304-3991. http://dx.doi.org/10.1016/0304-3991(94)90092-2. (Cited on page 18.)

[58] Jiang, Y. *et al. Electron ptychography of 2D materials to deep sub-ångström resolution*. Nature, **559**(7714):343–349 (2018). ISSN 1476-4687. http://dx.doi.org/10.1038/s41586-018-0298-5. (Cited on page 19.)

[59] Chen, Z. *et al. Mixed-state electron ptychography enables sub-angstrom resolution imaging with picometer precision at low dose*. Nature Communications, **11**(1):2994 (2020). ISSN 2041-1723. http://dx.doi.org/10.1038/s41467-020-16688-6. (Cited on page 19.)

[60] Claus, D. *et al. Dual wavelength optical metrology using ptychography*. Journal of Optics, **15**(3):035702 (2013). ISSN 2040-8978, 2040-8986. http://dx.doi.org/10.1088/2040-8978/15/3/035702. (Cited on page 19.)

[61] Du, M. *et al.* *Measuring laser beam quality, wavefronts, and lens aberrations using ptychography.* Optics Express, **28**(4):5022–5034 (2020). ISSN 1094-4087. http://dx.doi.org/10.1364/OE.385191. (Cited on page 19.)

[62] Gao, S. *et al.* *Electron ptychographic microscopy for three-dimensional imaging.* Nature Communications, **8**(1):163 (2017). ISSN 2041-1723. http://dx.doi.org/10.1038/s41467-017-00150-1. (Cited on page 19.)

[63] Li, P. and Maiden, A. *Multi-slice ptychographic tomography.* Scientific Reports, **8**(1):2049 (2018). ISSN 2045-2322. http://dx.doi.org/10.1038/s41598-018-20530-x. (Cited on page 19.)

[64] Dierolf, M. *et al.* *Ptychographic X-ray computed tomography at the nanoscale.* Nature, **467**(7314):436–439 (2010). ISSN 1476-4687. http://dx.doi.org/10.1038/nature09419. (Cited on page 19.)

[65] Shemilt, L. *et al.* *Karyotyping human chromosomes by optical and X-ray ptychography methods.* Biophysical Journal, **108**(3):706–713 (2015). ISSN 1542-0086. http://dx.doi.org/10.1016/j.bpj.2014.11.3456. (Cited on page 19.)

[66] Novotny, L. and Hecht, B. *Principles of Nano-Optics.* Cambridge University Press, Cambridge (2006). http://dx.doi.org/10.1017/CBO9780511813535. (Cited on page 23.)

[67] Godard, P. *et al.* *Noise models for low counting rate coherent diffraction imaging.* Optics Express, **20**(23):25914–25934 (2012). ISSN 1094-4087. http://dx.doi.org/10.1364/OE.20.025914. (Cited on pages 24 and 25.)

[68] Rottenfusser, R. *Proper Alignment of the Microscope.* In *Methods in Cell Biology*, volume 114, pages 43–67. Elsevier (2013). ISBN 9780124077614. http://dx.doi.org/10.1016/B978-0-12-407761-4.00003-8. (Cited on page 29.)

[69] Min, W. *et al.* *Coherent Nonlinear Optical Imaging: Beyond Fluorescence Microscopy.* Annual Review of Physical Chemistry, **62**(1):507–530 (2011). ISSN 0066-426X, 1545-1593. http://dx.doi.org/10.1146/annurev.physchem.012809.103512. (Not cited.)

[70] Diaspro, A. *et al.* *Photobleaching.* In J.B. Pawley, editor, *Handbook Of Biological Confocal Microscopy*, pages 690–702. Springer US, Boston, MA

(2006). ISBN 9780387259215 9780387455242. http://dx.doi.org/10.1007/978-0-387-45524-2_39. (Not cited.)

[71] Wang, L. *et al. Small-Molecule Fluorescent Probes for Live-Cell Super-Resolution Microscopy*. Journal of the American Chemical Society, **141**(7):2770–2781 (2019). ISSN 0002-7863. http://dx.doi.org/10.1021/jacs.8b11134. (Not cited.)